④

AD-A199 745

REPORT DOCUMENTATION PAGE		READ INSTRUCTIONS BEFORE COMPLETING FORM
1. REPORT NUMBER Acoustics & Vibration Laboratory No. 97457-1	2. GOVT ACCESSION NO. AD-A199 745	3. RECIPIENT'S CATALOG NUMBER
4. TITLE (and Subtitle) Development of a new wall shear stress gauge for fluid flows		5. TYPE OF REPORT & PERIOD COVERED Technical Report May 1986 through July 1988
		6. PERFORMING ORG. REPORT NUMBER
7. AUTHOR(s) Yuksel Gur and Patrick Leehey		8. CONTRACT OR GRANT NUMBER(s) N00014-86-K-0183
9. PERFORMING ORGANIZATION NAME AND ADDRESS Massachusetts Institute of Technology Cambridge, Massachusetts 02139		10. PROGRAM ELEMENT, PROJECT, TASK AREA & WORK UNIT NUMBERS ONR Code 11250A
11. CONTROLLING OFFICE NAME AND ADDRESS Office of Naval Research Underwater Acoustics Code 11250A Ballston Tower # 1 800 North Quincy St. Arlington, VA. 22217-5000		12. REPORT DATE August, 1988
		13. NUMBER OF PAGES 82
14. MONITORING AGENCY NAME & ADDRESS(if different from Controlling Office)		15. SECURITY CLASS. (of this report) Unclassified
		15a. DECLASSIFICATION/DOWNGRADING SCHEDULE

16. DISTRIBUTION STATEMENT (of this Report)

Approved for public release; distribution unlimited

17. DISTRIBUTION STATEMENT (of the abstract entered in Block 20, if different from Report)

18. SUPPLEMENTARY NOTES

19. KEY WORDS (Continue on reverse side if necessary and identify by block number)

Shear stress gauge

Stokes flow

20. ABSTRACT (Continue on reverse side if necessary and identify by block number)

See page 2 of this report

DD $_{1\ JAN\ 73}^{FORM}$ 1473   EDITION OF 1 NOV 65 IS OBSOLETE

DEVELOPMENT OF A NEW WALL SHEAR STRESS GAUGE FOR FLUID FLOWS

by

YUKSEL GUR and PATRICK LEEHEY

Report No. 97457-1

August, 1988

ACOUSTICS AND VIBRATION LABORATORY

Massachusetts Institute of Technology

Cambridge, Massachusetts 02139

DEVELOPMENT OF A NEW WALL SHEAR
STRESS GAUGE FOR FLUID FLOWS

by

Yuksel Gur and Patrick Leehey

ABSTRACT

A new technique has been developed to measure the wall shear
stress and its direction in the turbulent boundary layer. This technique
involves the measurement of torque upon a very small cylindrical body
placed above the wall deep in the viscous sublayer, so that the device is
operating in the creeping flow regime. The method of approach has
involved calibration tests on a gauge 8 mm. long by 0.8 mm. in diameter,
located in uniform shearing flow of glycerol created in a cone-and-plate
apparatus. Our theoretical, computational and experimental results show
that the torque has a linear relation with the wall shear stress. The gauge
response is reversed for reversing the flow. By directivity measurements
using this gauge, maximum wall shear stress direction and its magnitude
are obtained. Linear response is obtained up to Reynolds number 3.2
which was the highest we could get in our apparatus. We have used a
spectral element code, Nekton, for determining the creeping flow about
the gauge. There is a very good agreement between the experimental and
computational results.

TABLE OF CONTENTS

LIST OF FIGURES

NOMENCLATURE OF SYMBOLS

d	Cylinder diameter
F	Drag
h	Distance between wall and cylinder
H	Distance between stationary and moving walls
L	Length scale
L_s	Distance between stationary mirror and screen
N	Number of interpolation points around cylinder
p	Pressure
r	Radial distance
Re	Reynolds number, $\dfrac{U\,d^2}{\nu}$
T	Temperature
u	x component of velocity
$\vec{u}$	Velocity vector
U_∞	Free stream velocity
U	Constant shear rate
u_d	Disturbance velocity
$u_{d\ max.}$	Maximum disturbance velocity
u_*	Friction velocity, $\sqrt{\dfrac{\tau_w}{\rho}}$
u^+	$\dfrac{u}{u_*}$
v	y component of velocity
y	Distance from wall

y^+	Distance from wall in viscous units, $\dfrac{yu_*}{\nu}$
α	Angle between flow direction and normal direction of gauge
β	Cone angle
θ_T	Rotation angle of the gauge
μ	Absolute viscosity of fluid
ν	Kinematic viscosity of fluid
δL	Laser displacement
ρ	Fluid density
ω	Angular velocity of cone
ε	Aspect ratio, $\dfrac{h}{d}$
ε_l	Aspect ratio, $\dfrac{L}{d}$
σ	Variance
τ_w	Wall shear stress
$\vec{\tau}$	Stress vector
τ_{ij}	Stress tensor
τ_{rr}	Normal viscous stress in radial direction
$\tau_{\theta\theta}$	Normal viscous stress in tangential direction
$\tau_{r\theta}$	Viscous shear stress
ψ	Stream function
ξ, η	Bipolar coordinates
η_d	Ratio of the computational drag to analytical drag
η_t	Ratio of the computational torque to analytical torque

1. INTRODUCTION :

The measurement of mean and fluctuating shear stresses created on the wall under a turbulent boundary layer flow is very important in analyzing a flow field.

A variety of techniques such as the Stanton tube, the Preston tube, the surface fence, the floating element and the thermal methods have been used for the measurement of wall shear stress in a turbulent boundary layer. Stanton(1920) used a rectangular pitot tube, mounted on a wall in a fully developed laminar flow, and used the difference between the pressure measured with this pitot tube and the static pressure to determine the velocity at the center of the tube , and established that if the center of the Stanton tube was located close enough to the wall, the wall shear stress could be calculated as $\tau_w = \mu \dfrac{u(y)}{y}$. This is an indirect measurement technique. Preston, J.H.(1953) used a round pitot tube on a surface in the fully developed turbulent pipe flow and established a calibration curve for a round pitot tube. The surface fence that consists of a wall obstruction was invented by Konstantinov and Dragnysh(1955) . The difference in pressure before and behind this gauge is related to the wall shear stress. The advantages of this gauge over the Stanton tube is that it gives a doubled pressure reading. Head and Rechenberg,(1962) calibrated a surface fence and a Preston tube in a turbulent flow and compared these two gauges. Although there was an agreement in moderately unfavorable pressure gradients, the two gauges indicated different values of the wall shear stress in strongly unfavorable pressure gradients. Vagt, J.D. and Fernholtz, H.(1973) calibrated the surface fence versus the Preston tube and gave a calibration curve of the surface fence for the flow direction. The floating element technique based on the measurement of skin friction forces, acting on a floating element buried in the wall inside a turbulent boundary layer. Frei, D. and Thomann, H.(1980) used the floating element technique to investigate the error of Preston tubes in adverse pressure gradients. The gaps between the floating element and the surrounding wall filled with a liquid in order to prevent disturbing forces on the element. Petri, S.(1984) developed a 4 mm. by 4 mm. floating element to measure the wall shear stress. Although that gauge was satisfactory in operation, it did not provide the desired frequency response. The main difficulty with this technique is the gap effects.

The gap creates a disturbance field which affects the performance of the gauge. Another method of measuring the wall shear stress is the use of flush mounted hot film probes. The operation principle of these probes is that the fluid at the surface of the probe, which is mounted on a wall inside a turbulent boundary layer, is controlled at a specific temperature, which is different from that in the bulk fluid and the heat transfer rate between the fluid and the probe is measured. Using a calibration curve given between the measured heat transfer rate and the velocity , the wall shear stress can be determined. This technique measures the mean wall shear stress as well as fluctuating wall shear stress in a turbulent boundary layer.

Most of these techniques have limited applicability, and lack analytical and computational fluid studies for the gauges. We have developed a new technique for the measurement of the wall shear stress in a turbulent boundary layer. The measurement principle of this technique is to place a cylindrical body inside the viscous sublayer and measure the torque acting on the body. The gauge operates in the creeping flow regime by its inside the viscous sublayer. The torque acting on the gauge due to the linear shear flow of the viscous sublayer has a linear response to the wall shear stress. This is a direct measurement technique. Since the gauge has a linear response to the wall shear stress, both mean and fluctuating components of the wall shear stress can be measured. Another important feature of the gauge is that the gauge gives the maximum wall shear stress direction and its magnitude. This gauge could also be used to determine the flow direction.

2. ANALYTICAL PART

2.1. Wall shear stress device for viscous sublayer :

Our measurement technique for the wall shear stress is put a cylindrical body very close to a wall inside the viscous sublayer and measure the torque acting on the body due to the shearing flow of the viscous sublayer.

The experimental results show that the viscous sublayer extends from the wall to $y^+ = 5$. In this region the mean velocity profile is linear ($u^+ = y^+$). Although the mean velocity profile within the sublayer is a linear velocity profile, the flow within it is not laminar, but accompanied by considerable irregular fluctuations. The Reynolds number based on the characteristic length y^+ and the velocity at y^+, has the following relation to y^+ :

$$Re = (y^+)^2 .$$

Were the gauge to extend to the edge of the viscous sublayer, the Reynolds number would become 25. Stokes flow can not exist for this Reynolds number, therefore, the gauge configuration should be such that the gauge stays below $y^+ = 1$.

2.2. Behavior of Stokes Flows :

The Navier-Stokes equations for incompressible flow are

$$\rho \left(\frac{\partial \vec{u}}{\partial t} + \vec{u}.\nabla \vec{u} \right) = -\nabla p + \mu \nabla^2 \vec{u} ,$$

$$\text{where} \qquad \nabla.\vec{u} = 0 .$$

Consider a flow field with characteristic length , L , and velocity , U_∞ . With the proper nondimensional distance $x_i^* = \frac{x_i}{L}$, velocities $u_i^* = \frac{u_i}{U_\infty}$ and pressure $p^* = \frac{p}{\mu \dfrac{U_\infty}{L}}$, the Navier-Stokes

equations become

$$\text{Re } \frac{D\vec{u}^*}{Dt} = -\nabla^* p^* + \nabla^{*2}\vec{u}^* \ ,$$

where $\text{Re} = \dfrac{U_\infty L}{\nu}$. For $\text{Re} \to 0$, these equations become the Stokes equations :

$$\nabla^* p^* = \nabla^{*2}\vec{u}^* \ .$$

All properties of a Stokes flow are governed by linear equations for p, u_i, the vorticity ω_i , and the stress tensor τ_{ij} . The linear property may be used in adding flow fields to produce new flows. For two-dimensional flow with a symmetry plane or axisymmetric flow, the streamlines are symmetric and all the other properties , $u_{i,} p$, ω_i , τ_{ij} , are antisymmetric with respect to the symmetry plane.

2.3. Description of the problem :

Our measurement principle for the wall shear stress is to put a cylindrical body very close to a wall inside the viscous sublayer where the flow can be assumed to be a shearing flow and to measure the torque acting on the body. Therefore, our analytical and numerical studies are aimed at solving the creeping flow equations when there is a linear shear flow and a cylindrical gauge which is very close to a wall.

We expect the following functional relations for the torque T and the drag F per span acting on the cylindrical body with axis parallel to a plane wall due to a two-dimensional shearing flow directed parallel to the wall and normal to the cylinder axis :

$$T = f \ (\mu, Ud, d, h) \ ,$$

$$F = g \ (\mu, Ud, d, h) \ ,$$

where U ,d ,μ ,h are the constant shear rate, the diameter of the cylinder, the absolute viscosity and the distance between the wall and cylinder, respectively. Since we consider a Stokes flow , density does not appear as a variable in the above functional relations. Using the Buckingham π-theorem, these functional relations become

$$\frac{T}{\mu U d^2} = f_2(\frac{h}{d}),$$

$$\frac{F}{\mu U d} = g_2(\frac{h}{d}).$$

As can be seen, the torque and drag are linearly related to the wall shear stress $\tau_w = \mu U$. For a three-dimensional flow field , there is one more variable, the length scale of the cylinder L . For this case, the functional relations become

$$\frac{T}{\mu U d^2} = f_3(\frac{h}{d}, \frac{L}{d}),$$

$$\frac{F}{\mu U d} = g_3(\frac{h}{d}, \frac{L}{d}).$$

2.4. 2-D Solution of the Stokes equation for the cylindrical gauge :
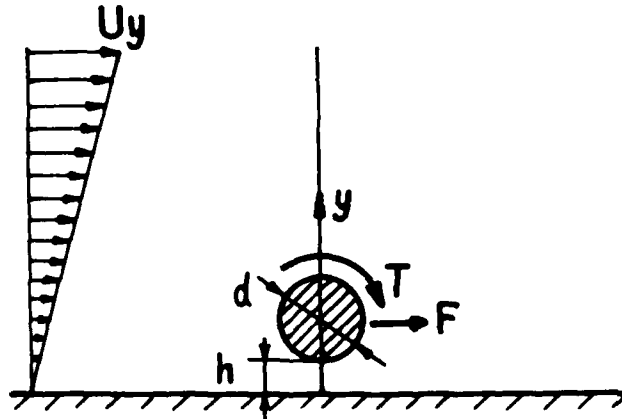

Figure (1). Cylindrical gauge

The solution of the Stokes equation, when there is a linear shear flow and a cylindrical gauge which is very close to a wall, was obtained by Davis and O'Neill(1977) by using a stream function formulation. Inflow velocity components were taken as (Uy, 0, 0). The equation of continuity is

$$\nabla.\vec{u} = 0 \ .$$

Using the stream function, ψ , velocities are given by

$$\vec{u} = (\ U\frac{\partial\psi}{\partial y} \ , -U\frac{\partial\psi}{\partial x} \ , 0 \ ) \ .$$

The boundary conditions are

$$\text{on the plane,} \qquad \psi = \frac{\partial\psi}{\partial y} = 0 \ ,$$

$$\text{on the cylinder,} \qquad \psi = M \quad , \quad \frac{\partial\psi}{\partial n} = 0 \ .$$

The constant M depends on the gap ratio, $\dfrac{h}{d}$, and can be determined from the flux of fluid through the gap. The boundary condition at infinity is $\psi \approx \frac{1}{2}y^2$ ($y \rightarrow \infty$). The equations of motion for Stokes flow are

$$\nabla p = \mu\nabla^2\vec{u} \ .$$

Using the stream function, the equations of motion become a biharmonic equation for ψ :

$$\nabla^4 \psi = 0.$$

The Reynolds number for the flow is $\dfrac{Ud^2}{4v}$. The Stokes solution is the lowest order asymptote as this Reynolds number approaches zero. Davis and O'Neill obtained the solution of this biharmonic equation in terms of bipolar coordinates. Their results show that the torque and drag force due to a linear shear flow are linearly related to the wall shear stress. Their solutions give the dimensional torque and drag on the body per unit length as

$$T = \frac{\pi}{2} \tau_w \, d^2 ,$$

$$F = 2 \pi \tau_w \, d \, (1 + \frac{2}{3}\varepsilon - \frac{4}{45}\varepsilon^2 + \cdots) ,$$

where $\varepsilon = \dfrac{h}{d}$. The drag equation agrees in terms of functional dependency with the result, found in section (2.3) using a dimensional analysis. An interesting result is that the torque acting on the body is independent of the gap. The pressure and shear stress are antisymmetric with respect to symmetry axis. As can be seen from the following figure, y components of the pressure and shear stress terms at θ and $-\theta$ cancel each other, therefore, the integration of the shear stress and pressure on the cylinder gives zero lift force.
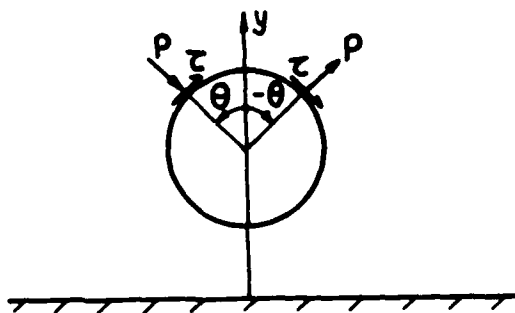
According to analytical results of Davis and O'Neill when the gap is approximately 0.685 times the cylinder radius or less, the flow first separates symmetrically from the wall. As the gap is further decreased to zero, symmetrical separations occur alternately on the body and the wall. The flow path between the body and the wall becomes increasingly tortuous. Flow visualization of an early stage of this process was done by Taneda(1979), see Figure 11 . In his experiment, the gap was 0.57 times the cylinder radius and Reynolds number was 0.011 .

2.5. Maximum Disturbance Velocity :

We measure the wall shear stress using a cylindrical gauge. It is necessary to know the disturbance velocity due to the cylindrical gauge to determine the proper size of the cylinder gauge for the wall shear stress measurements in the turbulent boundary layer. Another reason for investigating the disturbance velocity is that we use a cone-and-plate apparatus for testing the gauge; it consists of a stationary wall as well as a moving upper wall within which the gauge creates a blockage effect. The blockage effect due to the upper wall is important since the presence of the moving upper wall increases the velocity gradient on the cylinder, therefore, increasing the torque acting on the body. Decreasing the distance between the walls increases the torque. The disturbance velocity u_d is defined as the difference between the inflow velocity at y location ($U \ y$) and the velocity in the presence of the cylindrical body at the same location. When there is no body in the domain, the streamlines are straight lines. The streamlines take symmetrical curved shapes in the presence of the cylindrical body and the maximum disturbance velocity $u_{d \ max}$. occurs along the symmetry axis because of the presence of only x component of the velocity. Finite span decreases this velocity, hence the two dimensional calculation yields a conservative estimate of blockage. The maximum disturbance velocity is obtained using Davis and O'Neill's stream function formulation. The maximum disturbance velocity is derived in Appendix (A) and it is plotted in Figure 2 . It can be seen from Figure 2 that the maximum disturbance velocity decays almost exponentially in the y direction, and it is negligibly small when the distance from the wall is about 12 times the diameter plus the gap. The original cone-and-plate experiments

were done for four different values of $\dfrac{H}{d+h}$ = 2.355, 3.548, 4.754, 7.167 . As can be seen in the

maximum disturbance velocity plot, the ratio of $\dfrac{u_{d\ max.}}{u}$ changes from 0.06 to 0.003 in our

experiments. In the above experiments, there is almost no secondary flow effect since Reynolds

number is very small, but there is a blockage effect due to small gap heights H . In order to

prevent the blockage effect, the cone-and-plate experiments were done with an additional 12^0

cone for values of $\dfrac{H}{d+h}$ = 9.68 , 11.54 . In the 12^0 cone experiments, there is a significant

secondary flow effect because of having high Reynolds numbers. The Reynolds number

$\hat{R} = \dfrac{r^2 \omega \beta^2}{12\ v}$ ranges from 0.19 to 0.43 . Increasing Reynolds number increases the centrifugal

force in the cone-and-plate apparatus ; therefore, the streamlines at the stationary plate surface are

oriented more towards the center of the plate. The secondary flow effects in the experiments is

calculated according to H.P. Sdougos et al. (1984) and used to convert the experimental results to

actual calibration curves. The secondary flow effects will be discussed in details in section (3.1).

As can be seen in section (3.3), there is no blockage effects in the 12^0 cone-and-plate experiments

when the secondary flow correction is used. Therefore, we can conclude that the calibration curve

obtained with the 12^0 cone-and-plate experiments can be used as the calibration curve of the

gauge for boundary layer measurements.

Our experimental and theoretical flow calculations show that for the calibration of the

gauge, the cone angle should be such that the value of $\dfrac{H}{d+h}$ is bigger than 12 in order to

prevent blockage effects. If secondary flow effect is significant, the secondary flow correction

explained in section (3.3) should be made in order to get an actual calibration curve for boundary
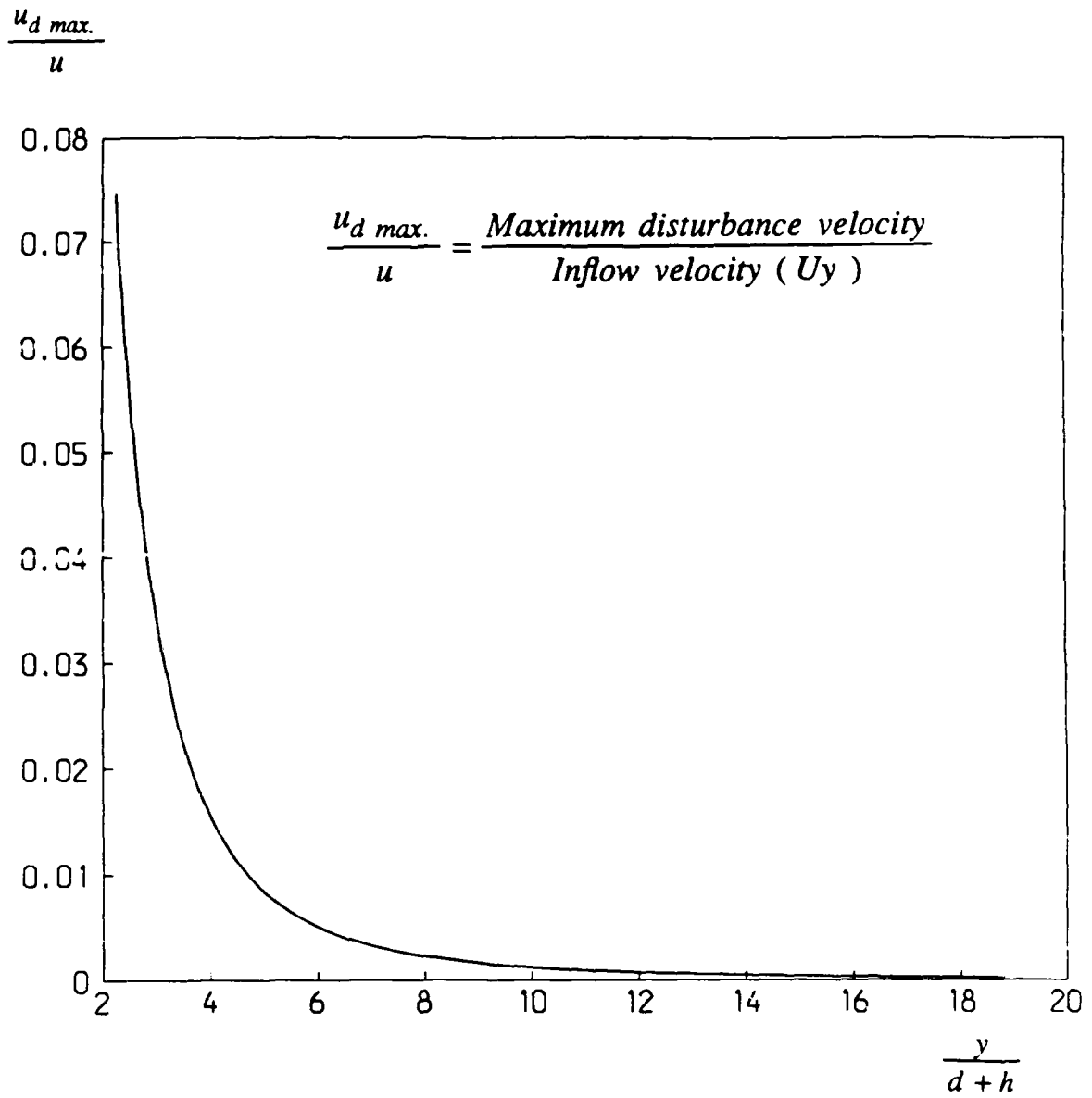
layer measurements.

Figure (2). Maximum disturbance velocity

3. EXPERIMENTAL SET-UP AND RESULTS :

3.1. Cone-and-plate apparatus and flow behavior in the apparatus :

The cone-and-plate apparatus used for the calibration of the cylindrical gauge is shown in Figure 9 . This apparatus was developed by Prof. C.F. Dewey, Jr. of M.I.T. The reason for using this apparatus is that it creates a linear shear flow and gives a constant shear rate everywhere inside the apparatus. The cone-and- plate apparatus consists of a shallow rotating cone and a stationary circular plate. The diameter of the apparatus used in the experiment is 206 mm.. Three different cones (3^0 , 6^0 and 12^0) are used in the experiment to determine the blockage effect. This apparatus is filled with glycerol or glycerol-water mixtures and driven by an electrical motor.

For small Reynolds numbers (Re $\ll$ 1), flow streamlines inside the apparatus are concentric circles and cone surface velocity, $u(r)$, increases linearly with radius. The wall shear stress is

$$\tau_w = \mu \frac{\partial u}{\partial y} ,$$

$$\tau_w = \mu \frac{\omega r}{H} = \mu \frac{\omega}{\tan\beta} .$$

For small cone angle, β, the wall shear stress is

$$\tau_w = \mu \frac{\omega}{\beta} ,$$

where β is the cone angle, μ is the absolute viscosity , ω is the angular velocity of the cone , and H is the gap heigth. The wall shear stress is constant everywhere inside the cone for small Reynolds numbers.

The flow behavior inside the cone-and-plate apparatus were investigated by H.P Sdougos, S.R. Bussolari, and C.F.Dewey,Jr.(1984). They investigated the flow behavior inside the cone-

and-plate apparatus using flow visualization, hot film heat-transfer probes and measurements of the torque required to rotate the cone against the retardation of the viscous fluid. They also presented theoretical results to these experiments. According to their findings , flow regimes are well characterized by the single dimensionless parameter:

$$\hat{R} = \frac{r^2 \omega \beta^2}{12 \nu}$$

where r is the radial distance from the axis of the cone. The parameter $\hat{R}$ is analogous to Reynolds number. They found a good agreement between the theoretical results of the wall shear stress values for $\hat{R} > 0.5$ and observed turbulence due to secondary flow for $\hat{R} \geq 4$. They did not attempt to describe the flow near the outer rim of the cone, where edge effects and the boundary conditions are important. The dimensionless parameter $\hat{R}$ is less than 0.02 in our 3^0 and 6^0 cone-and-plate experiments.

Fewell, M.E. and Hellums, J.D.(1977) investigated the secondary flow in cone-and-plate viscometers by numerical integration of the equations of motion for steady incompressible flow of Newtonian fluids. They assumed a spherical segment for the outer rim of the cone, and determined the effects of the Reynolds number and cone angle on secondary flow. They defined their Reynolds number as $\frac{R_0^2 \omega}{\nu}$, where R_0 is the outer radius of the cone. According to their results, there is no secondary flow effect in our experiments with 3^0 and 6^0 cone angles since the maximum Reynolds number $\frac{R_0^2 \omega}{\nu}$ is 39.5 in these experiments. Fewell's analysis can not say anything about the 12^0 cone experiments since the cone angle is not small enough for their analysis to be valid. We do not expect edge flow effects in our probe locations since the probe locations are not close to the edge of the cone. The probe locations are $0.49 R_0$ and $0.73 R_0$.

In order not to have the blockage effect which we have in the 3^0 and 6^0 cone-and-plate experiments, the cone-and-plate experiments have been done with an additional 12^0 cone. In the 12^0 cone-and-plate experiments, the secondary flow effect becomes very important since the

Reynolds number $\hat{R}$ is proportional to β^2. In the presence of secondary flow, the fluid streamlines are no longer concentric circles and fluid velocity vector forms an angle ϕ_s with the azimuthal direction. This angle was calculated by H.P.Sdougos et al. (1984) by using an expansion of the Navier-Stokes equations for small values of the single parameter $\hat{R} = \dfrac{r^2 \omega \beta^2}{12 \nu}$. They found the angle ϕ_s at the plate surface as

$$\phi_s = \tan^{-1}\frac{u}{v} = [-0.8\hat{R} + O(\hat{R}^3)] .$$

This expression is used for the 12^0 cone results with the experimental directivity curve, shown in Figure 20, to obtain an actual calibration curve for boundary layer measurements. In the 12^0 cone experiments, the Reynolds number $\hat{R}$ and ϕ_s are 0.19, -8.6^0 for $\dfrac{H}{d} = 13.4$ and 0.43, -19^0 for $\dfrac{H}{d} = 16$, respectively.

3.2. Construction of the gauge and measurement principle :

The cylindrical gauge is shown in Figure 4. The diameter of the gauge is 0.8 mm. and the length of the gauge is 8 mm.. The construction technique of this gauge was developed by Peter M. Wagner, research engineer from the Technische Universtat, Berlin. The gauge is made of platinum. One of its ends is polished flat with special polishing materials up to the centerline for an axial distance of 1.2 mm. in order to have a mirror surface for reflection of laser light used for sensing rotation. A plexiglass plate 50.8 mm. in diameter and 3.17 mm. in thickness is used for the mounting surface of the gauge. Four copper wires with a diameter of 0.4 mm. and a height of 0.6 mm. are mounted on the plexiglass as supports. Two platinum wires having a diameter of 25 micrometers are soldered to the supports after pretensioning. The gauge is also soldered at the center to the pretensioned platinum wires at both ends. The stationary plate of the apparatus has a diameter of 206 mm. and has a circular hole with a diameter of 50.8 mm. at a position 63 mm.

from the axis of the cone. The gauge on the plexiglass plate is put in the circular hole of the stationary plate of the apparatus. Glycerol and glycerol-water mixtures are used as working fluids in the apparatus in order to keep the Reynolds number small.

The measurement principle is basically shown in Figure 3. A stationary helium-neon laser sends a laser beam to a stationary mirror outside the apparatus. The reflected laser beam goes to the mirror surface of the gauge from the stationary mirror, and is reflected back to the stationary mirror. It then goes to a screen which is at a distance of 1 meter from the stationary mirror. When the cone does not rotate, there is a reference spot on the screen. When it rotates, it creates a linear shear flow. Due to that shearing flow the gauge rotates and the mirror surface of the gauge reflects the laser beam back at an angle. The reflected laser beam gives a displaced spot on the screen. We measure the displacement of the laser spot on the screen and measure the rotational speed ω of the cone at the same time using a digital counter. By measuring the rotational speed, we know the wall shear stress since $\tau_w = \mu \dfrac{\omega}{\beta}$. The relation between the rotation angle of the gauge and the laser displacement on the screen is

$$\delta L = 2 \, \theta_T \, L_s$$

where δL is the laser displacement, θ_T is the rotation angle of the gauge, and L_s is the distance between the stationary mirror and the screen. Basically, by measuring the rotational speed of the cone and the laser displacement, we get a calibration curve for wall shear stress versus the rotation angle of the gauge.
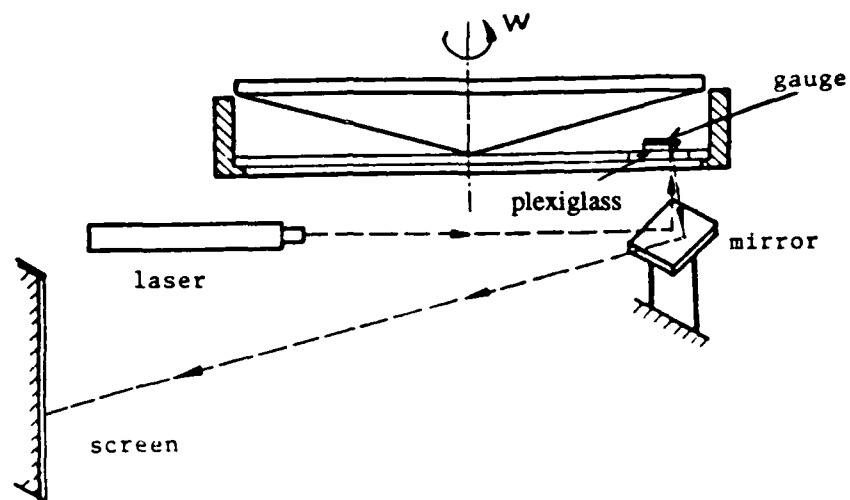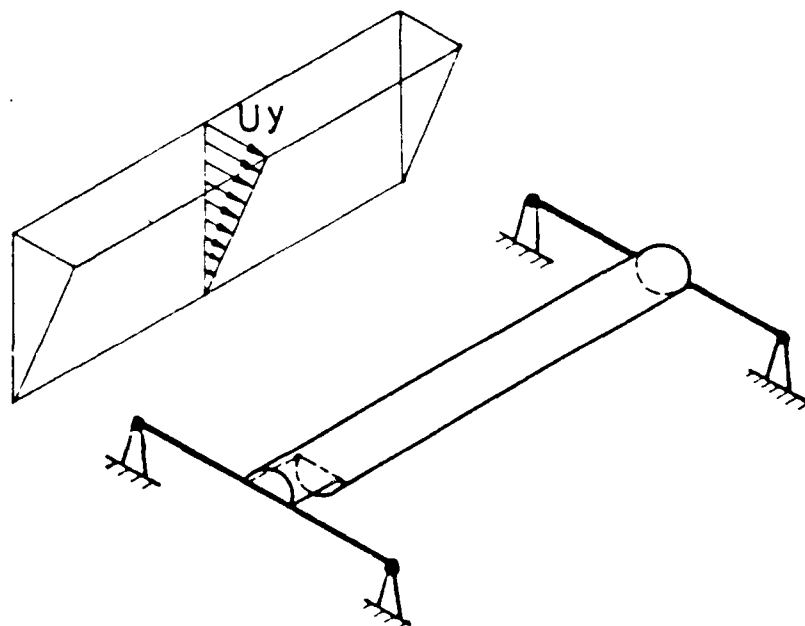
Figure (3). The cone-and-plate apparatus

Figure (4). Geometry of the shear stress gauge

3.3. Experimental Results :

As explained in section (3.1), the wall shear stress has a constant value over the plate surface of the cone-and-plate apparatus for small Reynolds numbers. In order to observe the blockage effect of the gauge, the same gauge is used in two different positions from the rotational axis of the cone for three different cones (3^0, 6^0, and 12^0). A linear response is obtained in each case.

The absolute viscosity of glycerol used in the experiment is 815 centipoise at the measurement temperature, 24^0C. The experimental result for the 3^0 cone and $\dfrac{H}{d} = 3.26$ is shown in Figure 12 . The average slope, the ratio of the laser displacement on the screen to the rotational speed of the cone, is 15.83 [mm.secs] and the ratio of the variance to the average slope is 7 % . The average slope in the measurement can be written as

$$Average\ slope = \frac{laser\ displacement}{rotational\ speed} = \frac{\delta L}{\omega} \ .$$

By putting the values δL and ω into above relation, we get the following relations

$$Average\ slope = \frac{2\,\mu\,L_s}{\beta}\,\frac{\theta_T}{\tau_w}$$

or

$$\frac{\tau_w}{\theta_T} = \frac{2\,\mu\,L_s}{\beta}\,\frac{1}{Average\ slope} \ .$$

Using the above relation, we find the ratio of the wall shear stress to the rotation angle of the gauge , $\dfrac{\tau_w}{\theta_T}$, as 34.30 [$N/m^2 deg.$] .

The experimental result for the 3^0 cone and $\dfrac{H}{d} = 4.91$ is shown in Figure 13 . The average slope, the ratio of the variance to the average slope, and the value of $\dfrac{\tau_w}{\theta_T}$ are 13.09 [mm. secs] , 3 % , and 41.49 [$N/m^2deg.$] respectively.

The experimental result for the 12^0 cone and $\dfrac{H}{d} = 13.4$ is shown in Figure 14 . The average slope is 1.81 [mm.secs] and the ratio of the variance to the slope is 4 % . The value of $\dfrac{\tau_w}{\theta_T}$ is 74.95 [$N/m^2deg.$].

The experimental result for the same cone angle, 12^0 , and the same viscosity , but the different gap, $\dfrac{H}{d} = 16$, is shown in Figure 15 . The average slope in this experiment is 1.63 [mm.secs] , and the ratio of the variance to the slope is 8 % , and the value of $\dfrac{\tau_w}{\theta_T}$ is 83.50 [$N/m^2deg.$].

Since the Reynolds number $\hat{R}$ is high in the 12^0 cone-and-plate experiments, secondary flow effects become very important. In the presence of secondary flow, the flow direction is no longer perpendicular to the symmetry axis of the gauge, and it forms an angle ϕ_s with the symmetry axis of the gauge. This angle is calculated as explained in section (3.1). We can assume that the torque acting on the gauge in the 12^0 cone experiments is only influenced by the wall shear stress on the plate since the position of the cone surface is far a way from the gauge ($\dfrac{H}{d} > 13$). By using this assumption, calculated values of ϕ_s , and the experimental directivity curve, we can obtain an actual ($\dfrac{\tau_w}{\theta_T}$) for subsequent boundary layer measurements. Basically, $\dfrac{\tau_w}{\theta_T}$ obtained in the cone-and-plate experiments is multiplied by the experimental direction sensitivity, shown in Figure 20, corresponding to ϕ_s in order to obtain an actual value of $\dfrac{\tau_w}{\theta_T}$. As can be seen from Table 2 , the values of $\dfrac{\tau_w}{\theta_T}$ obtained for the 12^0 cone at two different positions differ

by less than 2 % . The actual calibration result without blockage of the gauge is

$$\frac{\tau_w}{\theta_T} = 69.30 \ [N/m^2.deg. \ ].$$

The rotational stiffness of the gauge could not be measured, therefore, a constant rotational stiffness is assumed. This is a good assumption since the maximum rotation of the gauge in our experiments is around 2 [degree], and the response of the gauge is linear. Since we do not have the stiffness of the gauge, we can not compare the experimental torque results with the theoretical torque results.

As can be seen in Figure 16, the experimental values of $\frac{\tau_w}{\theta_T}$ decrease with decreasing gap height H hence the rotation angle θ_T of the gauge increases for constant shear stress τ_w . Decreasing the gap heigth increases the velocity gradient acting on the gauge thereby increasing the torque which is linearly related to the rotation angle of the gauge through the rotational stiffness of the gauge ($T = k_T \ \theta_T$, where k_t is the rotational stiffness of the gauge, and θ_T is the rotation angle of the gauge).

In each experiment, the measurements are taken both for positive and negative rotational speeds of the cone. As can be seen in Figures 12 through 15 , the gauge response is reversed upon reversing the flow direction. Therefore, the gauge gives the magnitude and direction of the wall shear stress. That is a very important feature of the gauge since most of the other techniques do not give the direction of the shear stress.

In order to see the direction sensitivity of the gauge, the angle between the flow direction and the normal to the symmetry axis of the gauge, α , is changed from 0^0 to 60^0 with 10^0 increments using the 3^0 cone for $\frac{H}{d} = 4.08$. The directivity measurements, shown in Figure 20, are obtained. If the flow field were two-dimensional , we would expect that only the velocity component normal to the gauge axis would generate a torque. In this case, the ratio of the wall shear stress at $\alpha = 0^0$ to the shear stress at α becomes $\cos(\alpha)$. The flow field can not be two-dimensional for our aspect ratio, $\varepsilon_l = 10$. Increasing the angle, α , increases the three dimension

effect in the flow field and gives more than a cosine effect. Up to $\alpha = 40^0$, the variance in the measured directivity resulting from repeated steady flow experiments remains small. A peak appears at $\alpha = 50^0$ with a very large variance. In some sense it is an "unstable point " since small changes from that angle give a very large difference in the response. It is likely that the gauge is deflected spanwise by cross-flow torque at large α. This would produce a complicated deformation of the gauge structure and a corresponding peculiarity in the behavior of the laser light sensing system. This behavior deserves more study. However, as it stands, the gauge should be capable of distinguishing moderate changes in flow direction as well as being able to determine a complete flow reversal.

In order to see up to what Reynolds number the flow field might be assumed a Stokes flow, glycerol-water mixtures with absolute viscosities ranging from 815 centipoise (100 % glycerol) to 32 centipoise (60 % glycerol , 40 % water in volume) are used. The maximum Reynolds number, which we could obtain in our cone-and-plate apparatus, based on the diameter of the gauge and shearing velocity at the gauge mid-section is 3.2 . Up to that Reynolds number, a linear response is obtained. These results are shown in Figures 21 through 23 . This indicates that the Stokes flow is a good engineering approximation up to a Reynolds number of at least

3.2 . This allows us to use that Reynolds number to determine the actual size of the gauge for wind tunnel and turbulent oil channel measurements.
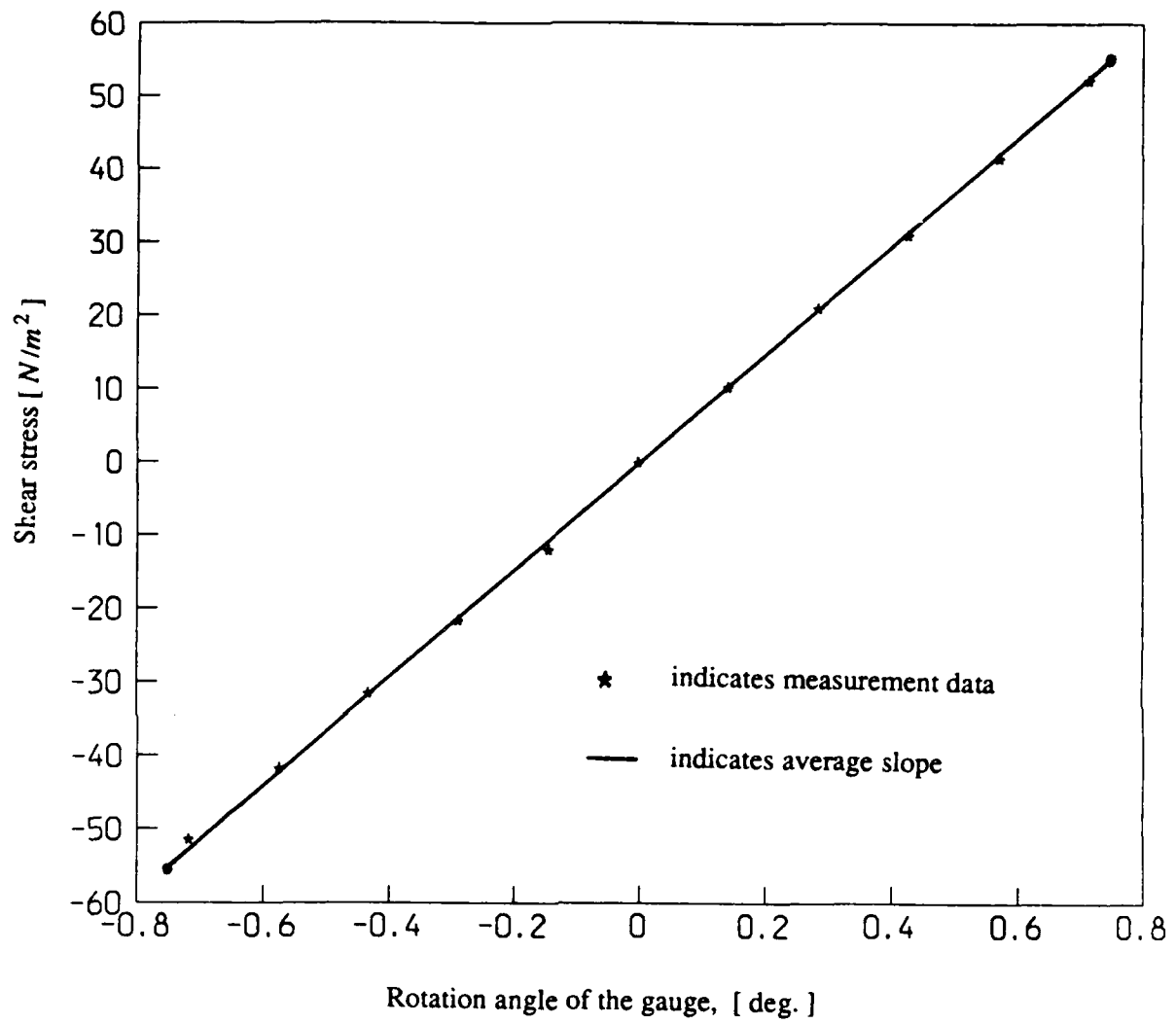
Figure (5). Experimental result for $\beta = 12^0$, $\frac{H}{d} = 13.4$

4. COMPUTATIONAL PART :

4.1. Introduction to the spectral element code, NEKTON :

We use the spectral element code, NEKTON , developed by Prof. A.T. Patera at M.I.T. , for computing the Stokes solution for the cylindrical gauge. NEKTON is a computer code for the simulation of steady and unsteady incompressible fluid flow with forced and natural convection heat transfer. The code has three parts: Prenek, Nekton and Postnek. Prenek is an interactive program in which all the necessary information for the flow problem such as geometrical, physical, and numerical parameter can be given. The Nekton part of the code performs the numerical integration of the Navier-Stokes and energy equations for the flow problem which is specified in Prenek. Postnek is an interactive graphic package , in which the results of a Nekton simulation can be analyzed.

The spectral element technique is a high order finite element technique. In the spectral element, the computational domain is broken up into macro elements as in the finite element technique and the velocity and pressure terms in each element are represented by high order Lagrangian interpolants. In each element, the velocity and pressure terms are expanded in terms of (N-1) th order polynomial Lagrangian interpolants through Chebyshev collocation points. Inserting the assumed forms of the dependent variables ($\vec{u}$, p , T) in the governing equations, and using weighted residual techniques, discrete equations are generated. The solution for the dependent variables, velocities, pressure, and temperature , are obtained at the collocation points of the mesh. Convergence to the exact solution can be obtained either by increasing the number of elements or by increasing the order of the interpolants.

We used the Stokes version of Nekton to compute the cylindrical gauge problem. The discretizations of steady and unsteady Stokes flows and their solution procedure are given by Ronquist, E.M. and Patera, A.T. (1988). In order to find the blockage effect of the gauge and compare the analytical solution of the torque and drag acting on the cylinder with computational results, the code is run for constant $\varepsilon = \dfrac{h}{d}$ and different values of $\dfrac{H}{d+h}$. The velocities and

pressure computed at collocation points are used in the approach, as explained in the appendix (B), to calculate the stress distribution around the cylinder. The torque and drag are then computed by integrating the shear stress and pressure terms over the cylinder.

4.2. Nondimensionalization of the problem :

We used the Stokes version of NEKTON to solve the steady Stokes equation for the cylindrical gauge.

The Stokes equation is

$$0 = - \nabla p + \mu \nabla^2 \vec{u}$$

By using the nondimensional distance $x_i^* = \dfrac{x_i}{d}$, velocities $u_i^* = \dfrac{u_i}{Ud}$, and pressure $p^* = \dfrac{p}{\mu U}$, the nondimensional form of the Stokes equation becomes

$$0 = - \nabla^* p^* + \nabla^{*2} \vec{u}^*$$

With this nondimensionalization, the nondimensional stress is

$$\tau^* = \frac{\tau}{\mu U}$$

The torque and drag equations in terms of nondimensional quantities becomes

$$T = \mu U \left[\frac{d}{2}\right]^2 \int_0^{2\pi} [\, \tau_{r\theta}^* |_{r=d/2} \,] \, d\theta ,$$

$$F = \mu U \frac{d}{2} \int_0^{2\pi} [\, (\tau_{r\theta}^* |_{r=d/2}) \cos\theta + p^* \sin\theta \,] \, d\theta .$$
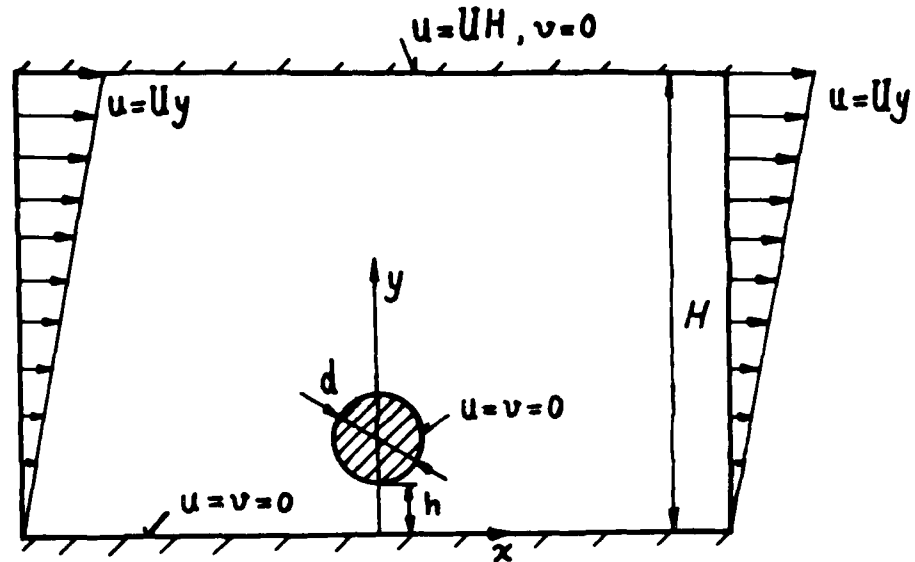
Figure (6). Computational domain

Figure 6 shows the boundary conditions for the problem. The inflow and outflow are taken as $u = Uy$, $v = 0$. Wall boundary conditions ($u = v = 0$) are specified on the cylinder and on the lower wall. On the upper wall the boundary conditions are $u = UH$, $v = 0$.

4.3. Computational results :

The computational domain, close to the cylinder, is broken up into circular elements in order to get the collocation data in the radial direction. By using this approach, we could easily convert the data, given in Cartesian coordinates by the code, to cylindrical coordinates, and compute the shear stress on the cylinder by using the approach given in Appendix (B). The other parts of the domain are broken up into rectangular elements. The size of the elements are decreased approaching the cylinder in order to increase the accuracy of the results. In the

computational calculation, the ratio ε of the gap (the distance between the cylinder and the lower wall) to the cylinder diameter is taken as a constant, $\varepsilon = 0.384$. The value of ε is chosen higher than the critical value, given by Davis and O'Neill for symmetrical flow separation. The code is run for constant $\varepsilon = 0.384$ and seven different values of $\dfrac{H}{d+h} = 2.355, 3.58, 4.754, 4.98, 7.167,$ 8.94, 12.77 . Two different orders of Lagrangian interpolants (5 th and 7 th order) are used. In each case, the shear stress on the cylinder, the torque and the drag are computed using the approach given in Appendix (B).

The velocity field for $\dfrac{H}{d+h} = 3.8$ is given in Figure 25 . In this figure, the vectors show the direction and magnitude of the velocities at the collocation points.

The spectral element mesh for $\varepsilon = 0.384$ and $\dfrac{H}{d+h} = 2.355$ is shown in Figure 26 . The shear stress distribution and pressure distribution on the cylinder are shown in Figure 28 and 29 , respectively. From these figures, the antisymmetric behavior of the shear stress and pressure can be seen. The maximum shear stress which appears at $\theta = 0^0$ is 9.68 times the wall shear stress τ_w and the minimum shear stress is $-2.70\,\tau_w$ at $\theta = 180^0$. The maximum pressure on the cylinder is $7.886\,\tau_w$.

The spectral element mesh for $\dfrac{H}{d+h} = 8.94$ and 7 th order Lagrangian interpolants is shown in Figure 37 . Figures 38 and 39 show the shear stress and pressure distributions on the cylinder. The maximum shear stress is $4.99\,\tau_w$ and the minimum shear stress is $-0.78\,\tau_w$. The maximum pressure is $3.42\,\tau_w$ at $\theta = 57^0$.

As can be seen from Table 1 , the maximum wall shear appears at $\theta = 0^0$. It decreases when the distance H between the lower and upper walls increases. The reason for this is that increasing H decreases the velocity gradient on the cylinder in order to maintain the constant flow rate. The shear stress starts decreasing from $\theta = 0^0$ and becomes zero at $\theta = 90^0$. After $\theta = 90^0$. the shear stress changes its direction, and starts increasing , and approaches an another extreme value at $\theta = 180^0$. The reason for this increase is that the geometry between the lower wall and cylinder

from $\theta = 90^0$ through 180^0 acts as a convergent channel, therefore, the velocity gradient has to increase while θ is increasing in order to maintain the constant flow rate. Parabolic velocity profiles are obtained in the region between the lower wall and cylinder. Another interesting point which should be mentioned is that the maximum pressure on the cylinder appears at $\theta = 57^0$.

The torque parameter η_t the ratio of the computational torque to analytical torque, is 1.941 for $\dfrac{H}{d+h} = 2.355$ and it is 1.044 for $\dfrac{H}{d+h} = 12.77$. The computational torque and drag results for each case are given in Table 1 and plotted in Figure 7 . As can be seen from Figure 7 , the computational torque and drag results approach exponentially to the analytical results as the distance H between the upper and lower walls is increased. This result validates the computational results since the analytical results are obtained for $H \rightarrow \infty$.
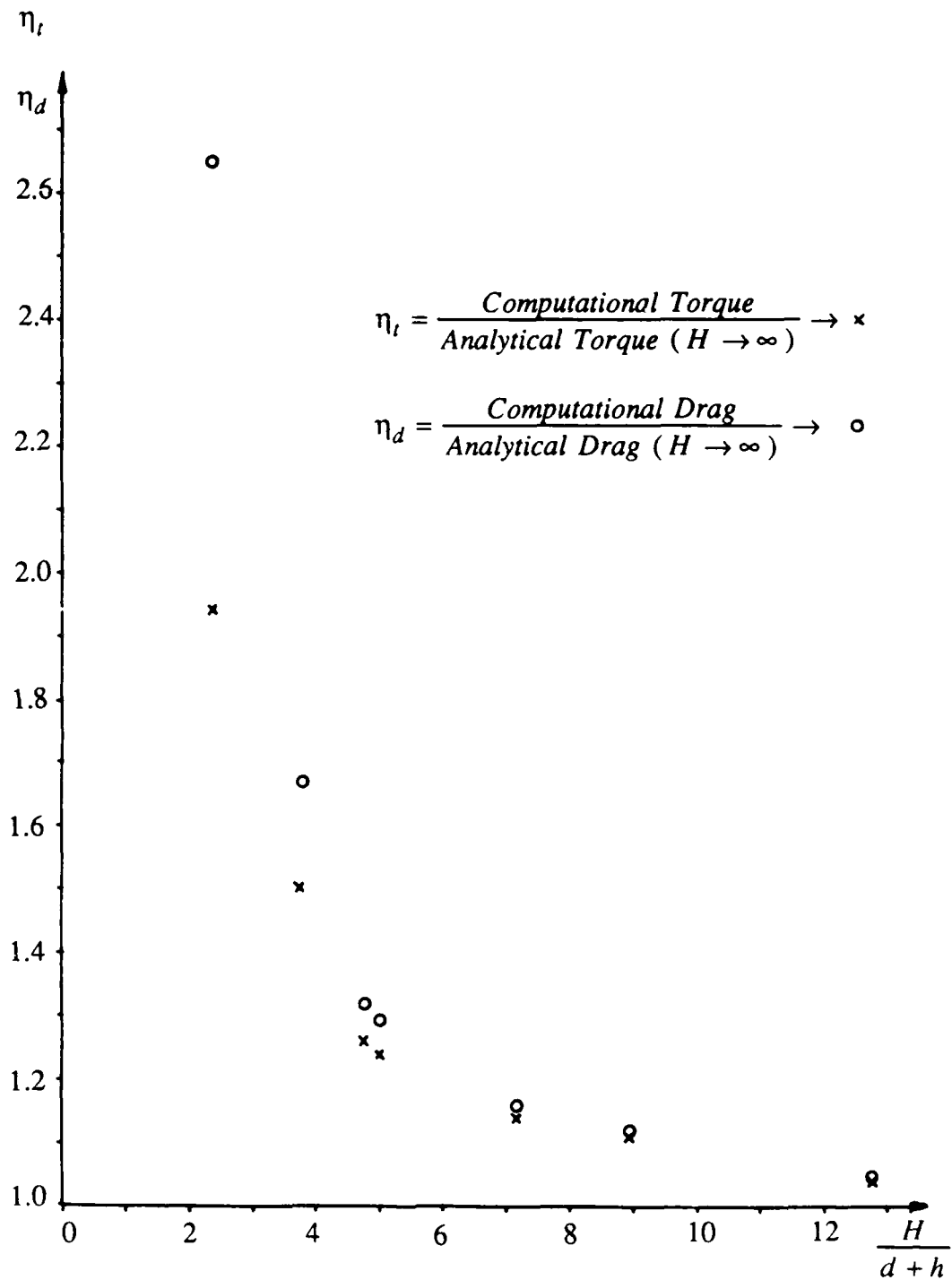
Figure (7). Computational torque and drag

5. CONCLUSIONS :

1. A new technique has been developed for the measurement of the wall shear stress in a turbulent boundary layer. The measurement principle is to place a cylindrical body deep inside the viscous sublayer and measure the torque acting on the body due to the shearing flow of the viscous sublayer.

2. The torque and drag force are linearly related to the wall shear stress.

3. The gauge diameter should be such that the gauge stays below $y^+ = 1$.

4. A gauge, 8 mm. long by 0.8 mm. in diameter, is calibrated and a linear response is observed.

5. By directivity measurements using this gauge, the maximum wall shear stress direction and its magnitude are obtained. That is a very important feature of the gauge since most of the other techniques do not give the direction of the shear stress.

6. A linear response is obtained up to the highest Reynolds number, 3.2, which we could get in our cone-and-plate apparatus. This result allows us to use that Reynolds number in order to determine the size of the gauge for wind tunnel and turbulent oil channel experiments.

7. The computational torque and drag results asymptote to the analytical results as the height H of the computational domain is increased. This corresponds to the experimental results.

8. For calibration of the gauge, the cone angle of the apparatus should be such that the value of $\dfrac{H}{d+h}$ is bigger than 12 in order to prevent blockage. If the secondary flow effect is significant, the secondary flow correction, explained in section (3.3) should be made in order to obtain the actual calibration curve for subsequent boundary layer measurements.

9. A three-dimensional solution of the creeping flow equations for the gauge is needed.

ACKNOWLEDGEMENTS :

REFERENCES

Davis, A.M. and O'Neill, M.E. 1977 : Separation in a slow linear Shear Flow Past a Cylinder and a Plane. J. Fluid Mech., vol. 81, part 3, 551-564

Fewell, M.E. and Hellums, J.D. 1977 : The Secondary Flow of Newtonian Fluids in Cone-and-Plate Viscometers. Trans. Soc. Rheol., vol. 21, 535-565

Frei, D. and Thomann, H. 1980 : Direct Measurements of Skin Friction in a Turbulent Boundary Layer with a Strong Adverse Pressure Gradient. J. Fluid Mech., vol. 101, part 1, 79-95

Goldstein, R.J. 1963 : Fluid Mechanics Measurements. Hemisphere, New York, N.Y.

Hasimoto, H. and Sano, O. 1980 : Stokeslets and Eddies in Creeping Flow. Ann. Rev. Fluid Mech., vol. 12, 335-363

Head, M.R. and Rechenberg, 1962 : The Preston Tube as a Means of Measuring Skin Friction. J. Fluid Mech., vol. 14, 1-17

Korczak, K.Z. and Patera, A.T. 1984 : A Spectral Element Method Applied to Unsteady Flows at Moderate Reynolds Number. in Proc. 9 th Int. Conf. on Num. Meth. in Fluid Dyn., Springer-Verlag, 314-319

NEKTON Users Manual 1987, MIT Fluid Mech. Lab.

Panton, R.L. 1984 : Incompressible Flow. Wiley-Interscience, New York, N.Y.

Petri, S.W. 1984 : Development of a Floating Element Wall Shear Transducer. Master of Science Thesis, MIT.

Preston, J.H. 1953 : The Determination of Turbulent Skin Friction by Means of Pitot Tubes. J. R. Aero.Soc., vol. 58, 109-121

Ronquist, E.M. and Patera, A.T. 1988 : A Legendre Element Method for the Incompressible Navier-Stokes Equations. to be published

Sdougos, H.P; Bussolari, S.R. and Dewey, C.F. 1984 : Secondary Flow and Turbulence in a Cone-and-Plate Device. J. Fluid Mech., vol. 138, 379-404

Taneda, S. 1979 : Visualization of Separating Stokes Flows. J. Phys. Soc. Japan, vol. 46, 1935-1942

Vagt, J.D. and Fernholz, H. 1973 : Use of Surface Fences to Measure Wall Shear Stress in Three Dimensional Boundary Layers. Aeronautical Quarterly, vol. 24, part 2, 87-91

Wagner, P.M. and Leehey, P. 1987 : A New Method for Measurement of Turbulent Wall Shear Stress. Proceedings of the 33 rd International Instrumentation Symposium, ISA. 363-372

White, F.W. 1974 : Viscous Fluid Flow. McGraw-Hill, New York, N.Y.

Winter, K.G. 1977 : An Outline of the Techniques Avaliable for the Measurement of the Skin Friction in Turbulent Boundary Layers. Prog. Aerospace Sci., vol.18, 1-57

APPENDIX (A) :

DERIVATION OF MAXIMUM DISTURBANCE VELOCITY :

The solution of the biharmonic equation for a cylinder close to a wall was given given by Davis and O'Neill (1977) in terms of bipolar coordinates. Bipolar coordinates can be obtained by considering the complex function for obtaining the potential for two opposite line sources a distance 2c apart :

$$W = \ln\left[\frac{(c+z)}{(c-z)}\right] = 2\tanh^{-1}(\frac{z}{c}) .$$ (A.1)

Using $W = \eta + i\xi$ and $z = x + iy = c\tanh[\frac{W}{2}]$, the Cartesian coordinates in terms of bipolar coordinates are obtained as

$$x = \frac{c\sin\eta}{\cosh\xi - \cos\eta} , \quad y = \frac{c\sinh\xi}{\cosh\xi - \cos\eta} .$$ (A.2)

with $c = \frac{d}{2}\sinh\alpha$. The plane is given by $\xi=0$ and the cylinder is given by $\xi=\alpha$. The solution of the biharmonic equation which satisfies the wall boundary conditions on the plane and on the cylinder and free stream flow boundary condition at infinity were given by

$$\psi = \frac{1}{2}y^2 - \chi + M\phi$$ (A.3)

where χ and ϕ

$$\chi = \frac{1}{2} (\frac{c}{d})^2 (\cosh\xi - \cos\eta)^{-1} \sum_{n=0}^{\infty} \chi_n(\xi) \cos n\eta \qquad (A.4)$$

$$\phi = (\cosh\xi - \cos\eta)^{-1} [\phi_0(\xi) + \phi_1(\xi) \cos\eta] \qquad (A.5)$$

with

$$\chi_0(\xi) = A_0 \xi\sinh\xi + B_0 (\xi\cosh\xi - \sinh\xi) \qquad (A.6a)$$

$$\chi_1(\xi) = A_1(\cosh2\xi - 1) + B_1(\sinh2\xi - 2\xi) \qquad (A.6b)$$

$$\chi_n(\xi) = A_n [\cosh(n+1)\xi - \cosh(n-1)\xi] + B_n [(n-1)\sinh(n+1)\xi \qquad (A.6c)$$

$$- (n+1)\sinh(n-1)\xi] \quad (n \geq 2)$$

$$\phi_0(\xi) = a_0 \xi\sinh\xi + b_0(\xi\cosh\xi - \sinh\xi) \qquad (A.6d)$$

$$\phi_1(\xi) = a_1(\cosh 2\xi - 1) + b_1(\sinh2\xi - 2\xi) . \qquad (A.6e)$$

The coefficients in the above equations are

$$a_0 = - \frac{\sinh^2\alpha}{\alpha^2 - \sinh^2\alpha} \quad , \qquad b_0 = \frac{\alpha + \sinh\alpha \, \cosh\alpha}{\alpha^2 - \sinh^2\alpha} \qquad \text{(A.7a)}$$

$$a_1 = - \frac{0.5 \tanh\alpha}{\alpha - \tanh\alpha} \quad , \qquad b_1 = \frac{0.5}{\alpha - \tanh\alpha} \qquad \text{(A.7b)}$$

$$A_0 = \frac{\alpha - \cosh\alpha \, \sinh\alpha}{\alpha^2 - \sinh^2\alpha} \quad , \qquad B_0 = \frac{\sinh^2\alpha}{\alpha^2 - \sinh^2\alpha} \qquad \text{(A.7c)}$$

$$A_1 = \frac{\alpha \, e^{-2\alpha} - e^{-\alpha} \sinh\alpha + \sinh^2\alpha}{\sinh 2\alpha \, (\alpha - \tanh\alpha)} \quad , \qquad B_1 = \frac{-0.5 \tanh\alpha}{\alpha - \tanh\alpha} \qquad \text{(A.7d)}$$

$$A_n = \frac{n(n - \coth\alpha)\sinh^2\alpha + e^{-n\alpha}\sinh n\alpha}{\sinh^2 n\alpha - n^2 \sinh^2\alpha} \quad , \qquad B_n = \frac{-n\,\sinh^2\alpha}{\sinh^2 n\alpha - n^2 \sinh^2\alpha} \quad (n \geq 2) \quad . \text{(A.7e)}$$

The x component of the velocity is

$$u = \frac{\partial\psi}{\partial y} = U \left(y - \frac{\partial\chi}{\partial y} + M \, \frac{\partial\phi}{\partial y} \right) \qquad \text{(A.8)}$$

where

$$\frac{\partial\chi}{\partial y} = \frac{\partial\chi}{\partial\xi} \, \frac{\partial\xi}{\partial y} + \frac{\partial\chi}{\partial\eta} \, \frac{\partial\eta}{\partial y} \qquad \text{(A.9a)}$$

$$\frac{\partial \phi}{\partial y} = \frac{\partial \phi}{\partial \xi} \frac{\partial \xi}{\partial y} + \frac{\partial \phi}{\partial \eta} \frac{\partial \eta}{\partial y} \quad . \tag{A.9b}$$

Partial derivatives of Cartesian coordinates with respect to bipolar coordinates are

$$\frac{\partial x}{\partial \xi} = - \frac{c \ \sin\eta \ \sinh\xi}{(\cosh\xi - \cos\eta)^2} \tag{A.10a}$$

$$\frac{\partial x}{\partial \eta} = \frac{c \ (\cos\eta \ \cosh\xi - 1)}{(\cosh\xi - \cos\eta)^2} \tag{A.10b}$$

$$\frac{\partial y}{\partial \xi} = \frac{c \ (-\cosh\xi \ \cos\eta + 1)}{(\cosh\xi - \cos\eta)^2} \tag{A.10c}$$

$$\frac{\partial y}{\partial \eta} = \frac{c \ (-\sin\eta \ \sinh\xi)}{(\cosh\eta - \cos\eta)^2} \quad . \tag{A.10d}$$

As can be seen from the above relations,

$$\frac{\partial y}{\partial \xi} = - \frac{\partial x}{\partial \eta} \quad , \quad \frac{\partial x}{\partial \xi} = \frac{\partial y}{\partial \eta} \quad . \tag{A.11}$$

The Jacobian is

$$J = \frac{\partial(x, y)}{\partial(\xi, \eta)} = \frac{\partial x}{\partial \xi} \frac{\partial y}{\partial \eta} - \frac{\partial y}{\partial \xi} \frac{\partial x}{\partial \eta} = (\frac{\partial y}{\partial \eta})^2 + (\frac{\partial y}{\partial \xi})^2 \quad . \tag{A.12}$$

By putting the derivatives in to the Jacobian and after some reduction,

$$J = \frac{c^2}{(\cosh\xi - \cos\eta)^2} .$$
(A.13)

Partial derivatives of bipolar coordinates with respect to Cartesian coordinates are

$$\frac{\partial\xi}{\partial x} = J^{-1}\frac{\partial y}{\partial\eta} \quad , \quad \frac{\partial\eta}{\partial x} = -J^{-1}\frac{\partial y}{\partial\xi} ,$$
(A.14a)

$$\frac{\partial\xi}{\partial y} = -J^{-1}\frac{\partial x}{\partial\eta} \quad , \quad \frac{\partial\eta}{\partial y} = J^{-1}\frac{\partial x}{\partial\xi} .$$
(A.14b)

By putting equation (A.13) into equation (A.14),

$$\frac{\partial\eta}{\partial x} = -\frac{\partial\xi}{\partial y} = \frac{1}{c}(\cosh\xi\cos\eta - 1) ,$$
(A.15a)

$$\frac{\partial\xi}{\partial x} = \frac{\partial\eta}{\partial y} = \frac{1}{c}(-sin\,\eta\,\sinh\xi) .$$
(A.15b)

The disturbance velocity u_d is the difference between the inflow velocity at y location (Uy) and the velocity in the presence of the cylindrical body. The maximum disturbance velocity occurs along the symmetry axis because of the presence of only x component of the velocity. In other words, the maximum displacement of each streamline due to the body occurs on the symmetry axis.

Bipolar coordinate η is zero on the y axis.

$$\frac{\partial \chi}{\partial \eta} = 0 \quad , \quad \frac{\partial \phi}{\partial \eta} = 0 \qquad at \ \eta = 0 \ . \tag{A.16}$$

Using equation (A.16) in the velocity equation (A.8), we obtain the velocity on the symmetry axis as

$$u_0 = U \ (y - \frac{\partial \chi}{\partial \xi} \frac{\partial \xi}{\partial y} + M \ \frac{\partial \phi}{\partial \xi} \frac{\partial \xi}{\partial y}) \qquad at \ \eta = 0 \ . \tag{A.17}$$

The maximum disturbance velocity is

$$u_{d \ max.} = u_0 - U \ y \ . \tag{A.18}$$

In terms of the stream function,

$$u_{d \ max.} = U \ (- \frac{\partial \chi}{\partial \xi} + M \ \frac{\partial \phi}{\partial \xi}) \ \frac{\partial \xi}{\partial y} \tag{A.19}$$

where

$$\frac{\partial \chi}{\partial \xi} = - \frac{1}{2} \ c^2 \ (\cosh\xi - 1 \ )^{-2} \sinh\xi \sum_{n=0}^{\infty} \chi_n(\xi) + \frac{1}{2} \ c^2 \ (\cosh\xi - 1 \ )^{-1} \sum_{n=0}^{\infty} \chi_n'(\xi) \tag{A.20a}$$

- 46 -

$$\frac{\partial \phi}{\partial \xi} = - (\cosh\xi - 1)^{-2} \sinh\xi \, [\, \phi_0(\xi) + \phi_1(\xi) \,] + (\cosh\xi - 1)^{-1} [\, \phi_0'(\xi) + \phi_1'(\xi) \,] \qquad \text{(A.20b)}$$

$$\frac{\partial \xi}{\partial y} = \frac{1}{c} (1 - \cosh\xi) \qquad \text{(A.20c)}$$

$$M \approx \frac{1}{4} d^2 \cosh^2\alpha \qquad \text{(A.20d)}$$

$$\chi_0'(\xi) = A_0 (\sinh\xi - \xi \cosh\xi) + B_0 \, \xi \sinh\xi \qquad \text{(A.20e)}$$

$$\chi_n' = A_n \, [\, (n + 1) \, sinh(n + 1)\xi - (n - 1)\sinh(n - 1)\xi \,] \qquad \text{(A.20f)}$$

$$+ B_n \, (n^2 - 1) \, [\, cosh(n + 1)\xi - \cosh(n - 1)\xi \,] \quad (n \geq 2)$$

$$\phi_0'(\xi) = a_0 (\sinh\xi + \xi \cosh\xi) + b_0 \, \xi \sinh\xi \qquad \text{(A.20g)}$$

$$\phi_1'(\xi) = a_1 \, 2 \sinh2\xi + b_1 \, 2 (\cosh2\xi - 1) \quad . \qquad \text{(A.20h)}$$

The other functions $\chi_0(\xi)$, $\chi_1(\xi)$, $\chi_n(\xi)$, $\phi_0(\xi)$, $\phi_1(\xi)$ and the coefficients in these functions are given in equations (A.6) through (A.7). The maximum disturbance velocity $u_{d\ max.}$ is computed and plotted in Figure 2.

APPENDIX (B) :

COMPUTATION OF TORQUE AND DRAG :

In this section the computational approach for determining torque and drag is given. The velocities, computed with NEKTON in Gaussian collocation points, are converted to cylindrical coordinates and then the closest three interpolation point velocities around the cylinder in radial directions are used in second order polynomials to find their variations in radial directions on the cylinder. The shear stress distribution on the cylinder is obtained by calculating the derivatives of the velocities. The torque and drag are calculated by integrating the shear stress and pressure on the cylinder.

For a Newtonian fluid, the viscous stress vector at the surface of a body must lie on the surface. Therefore, at the surface all the normal viscous stresses vanish. The only nonzero stress , $\tau_{r\theta}$, on the cylinder is

$$\tau_{r\theta}|_{r=d/2} = \mu \left[\frac{\partial u_\theta}{\partial r} \right]|_{r=d/2} \cdot \tag{B.1}$$

The torque and drag acting on the cylinder are

$$T = \int_0^{2\pi} [\tau_{r\theta}|_{r=d/2}] [\frac{d}{2}]^2 d\theta , \tag{B.2}$$

$$F = \int_0^{2\pi} [(\tau_{r\theta}|_{r=d/2}) \cos\theta + p \sin\theta] \frac{d}{2} d\theta . \tag{B.3}$$
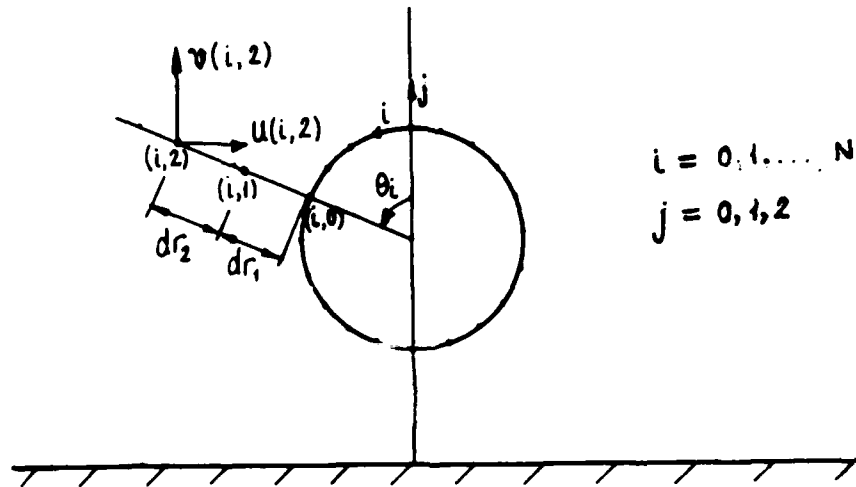
Figure (8). Velocities at the collocation points

The velocities in cylindrical coordinates in terms of Cartesian coordinates are

$$u_\theta(i,j) = u(i,j) \cos \theta_i + v(i,j) \sin \theta_i \ , \qquad \text{(B.4)}$$

$$u_r(i,j) = -u(i,j) \sin \theta_i + v(i,j) \cos \theta_i \ . \qquad \text{(B.5)}$$

Taking a second order polynomial for the radial velocity u_{θ_i} as

$$u_{\theta_i} = C_1 r^2 + C_2 r + C_3 \ , \qquad \text{(B.6)}$$

and using the values of $u_\theta(i,0)$, $u_\theta(i,1)$, $u_\theta(i,2)$ to find the coefficients, C_1, C_2, C_3, and after some manipulation, we get $\frac{\partial u_{\theta_i}}{\partial r}\big|_{r=d/2}$ as

$$\frac{\partial u_{\theta_i}}{\partial r}\Big|_{r=d/2} = \frac{1}{D_1}\left[dr_1{}^2 u_\theta(i,2) - (dr_1 + dr_2)^2 u_\theta(i,1)\right] \tag{B.7}$$

where

$$D_1 = -dr_1 dr_2 (dr_1 + dr_2) . \tag{B.8}$$

The shear stress on the cylinder in dimensional form is

$$\tau_{r\theta_i} = \mu\left[\frac{\partial u_{\theta_i}}{\partial r}\right]\Big|_{r=d/2} \tag{B.9}$$

The shear stress equation (B.9) is evaluated by using equation (B.7) and (B.8) .

The torque and drag equations in discrete form are

$$T = \sum_{n=0}^{N}\left[\frac{\tau_{r\theta_i} + \tau_{r\theta_{i+1}}}{2}\left[\frac{d}{2}\right]^2\left[\theta_{i+1} - \theta_i\right]\right] , \tag{B.10}$$

$$F = \sum_{n=0}^{N}\left[\frac{\tau_{r\theta_i} + \tau_{r\theta_{i+1}}}{2}\cos\left[\frac{\theta_{i+1} + \theta_i}{2}\right] + \frac{p_{i+1} + p_i}{2}\sin\left[\frac{\theta_{i+1} + \theta_i}{2}\right]\right]\frac{d}{2}\left[\theta_{i+1} - \theta_i\right] . \tag{B.11}$$
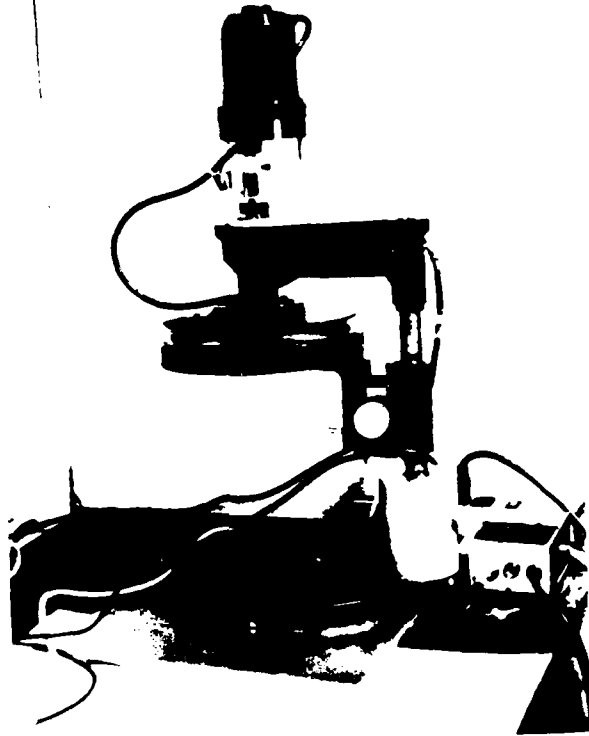
Figure (9). The cone-and-plate apparatus
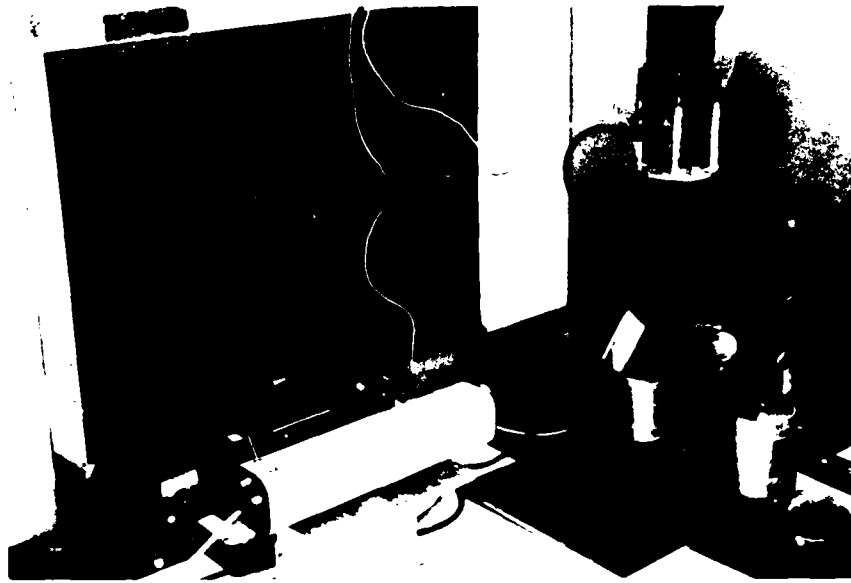
Figure (10). The shear stress gauge and experimental set-up
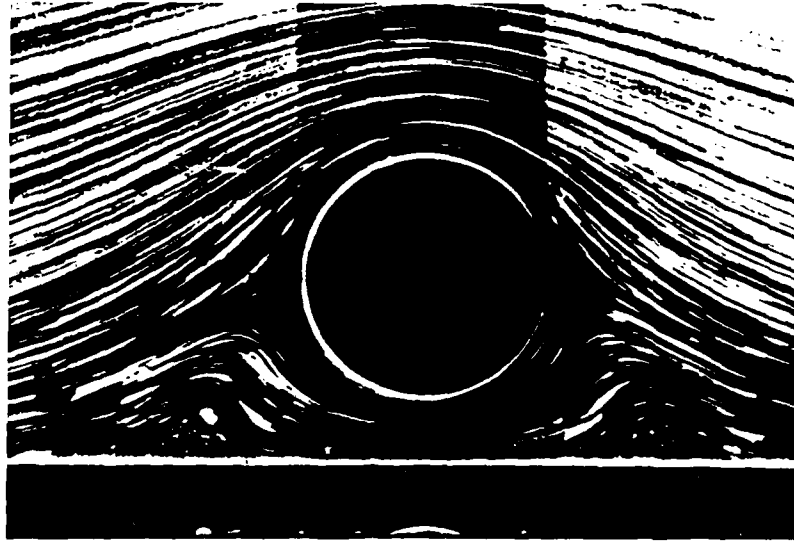
Figure (11). Shear flow over a cylinder near a wall, from Taneda(1979)
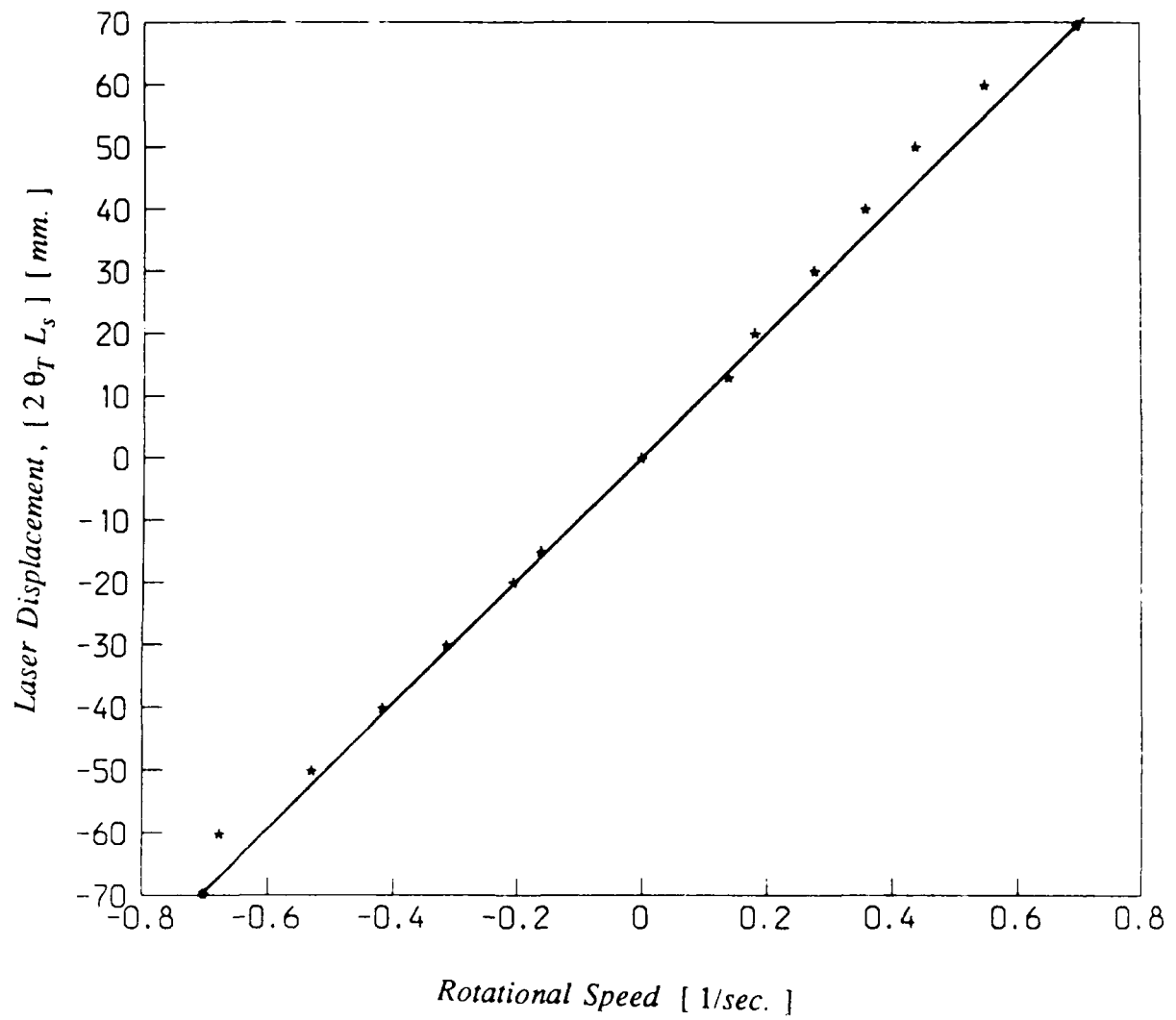
Figure (12). Experimental result for $\dfrac{H}{d} = 3.26$, $\beta = 3^0$
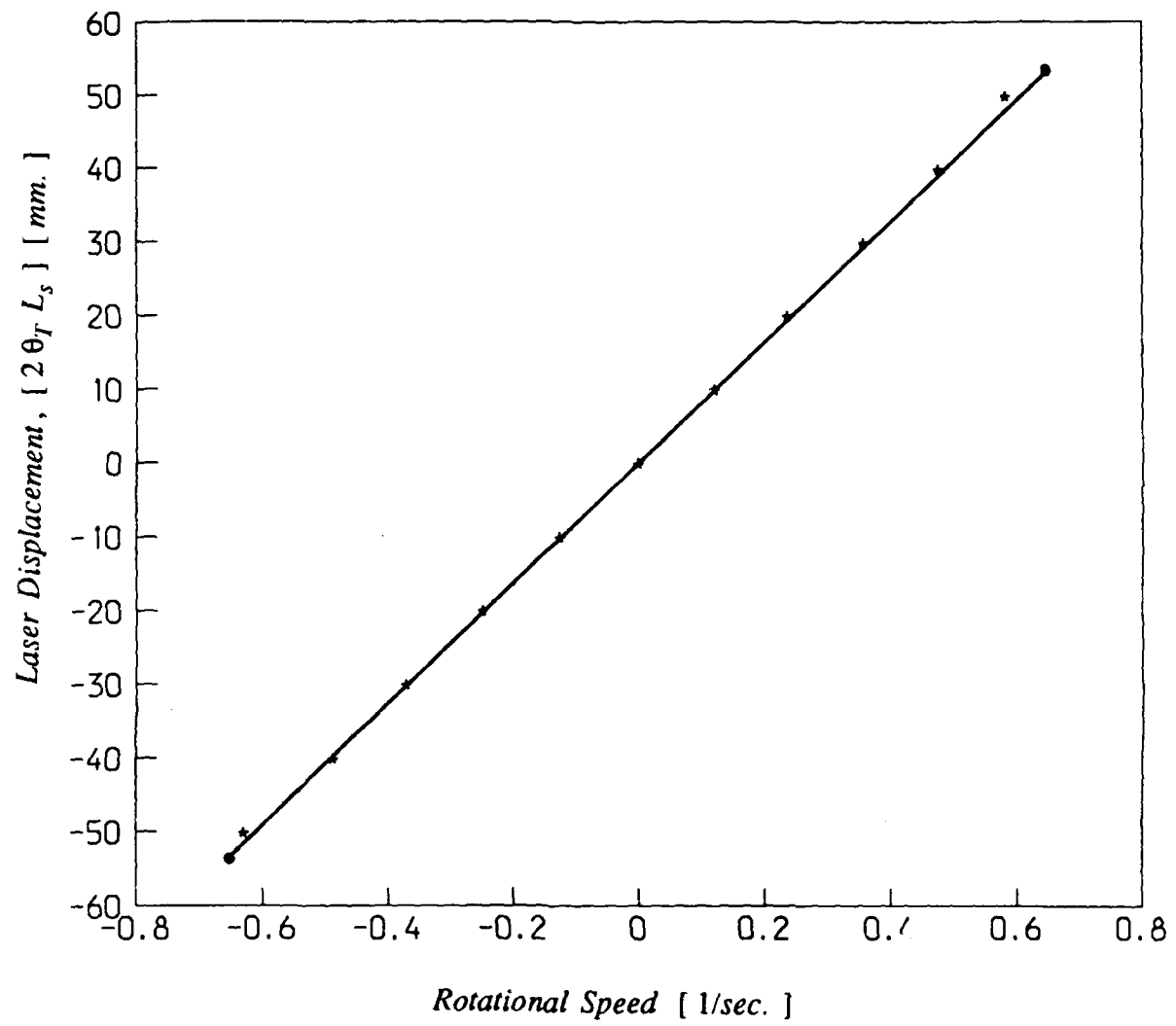
Figure (13). Experimental result for $\dfrac{H}{d} = 4.91$, $\beta = 3^0$
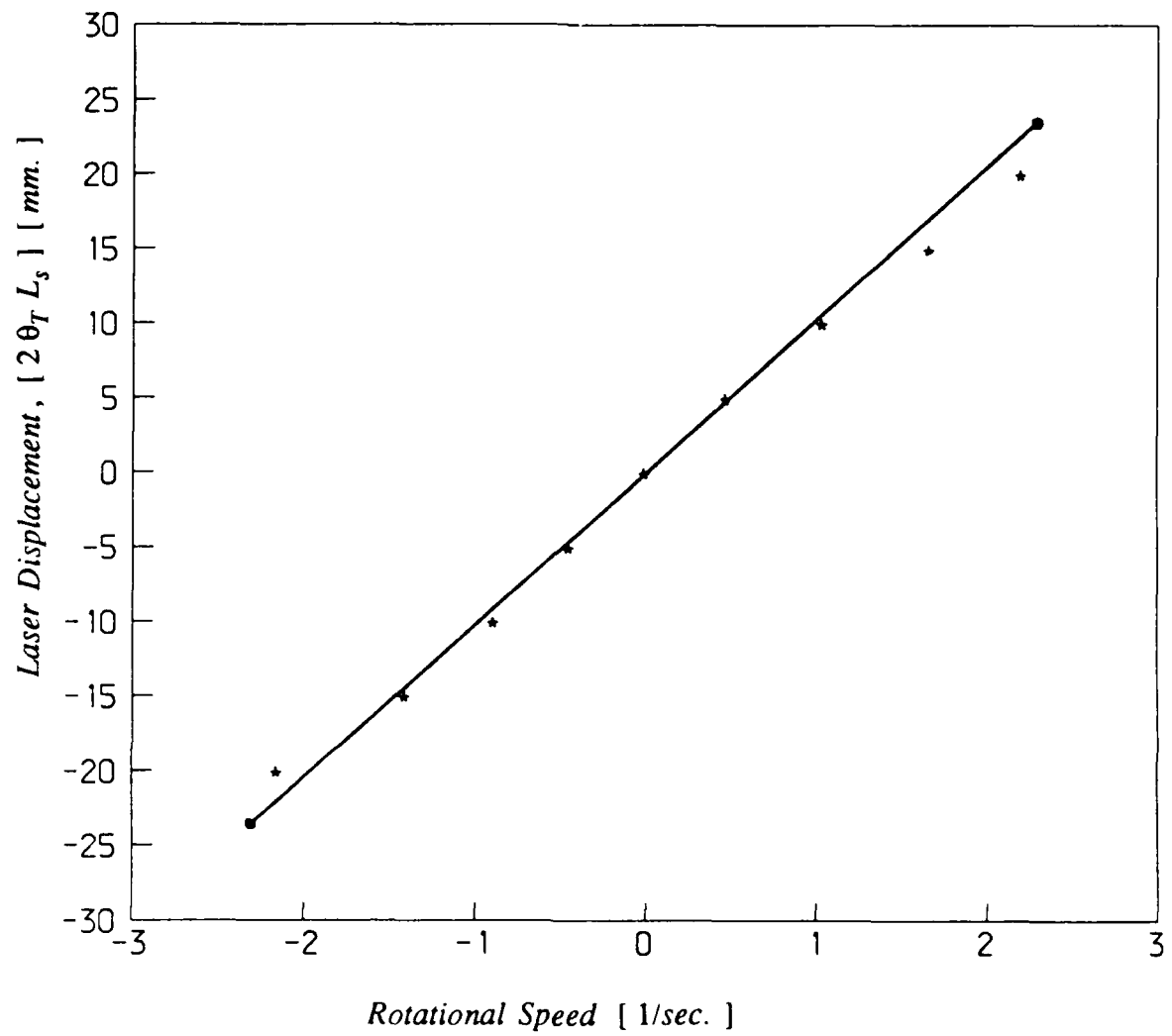
Figure (14). Experimental result for $\dfrac{H}{d} = 13.4$, $\beta = 12^0$

- 56 -
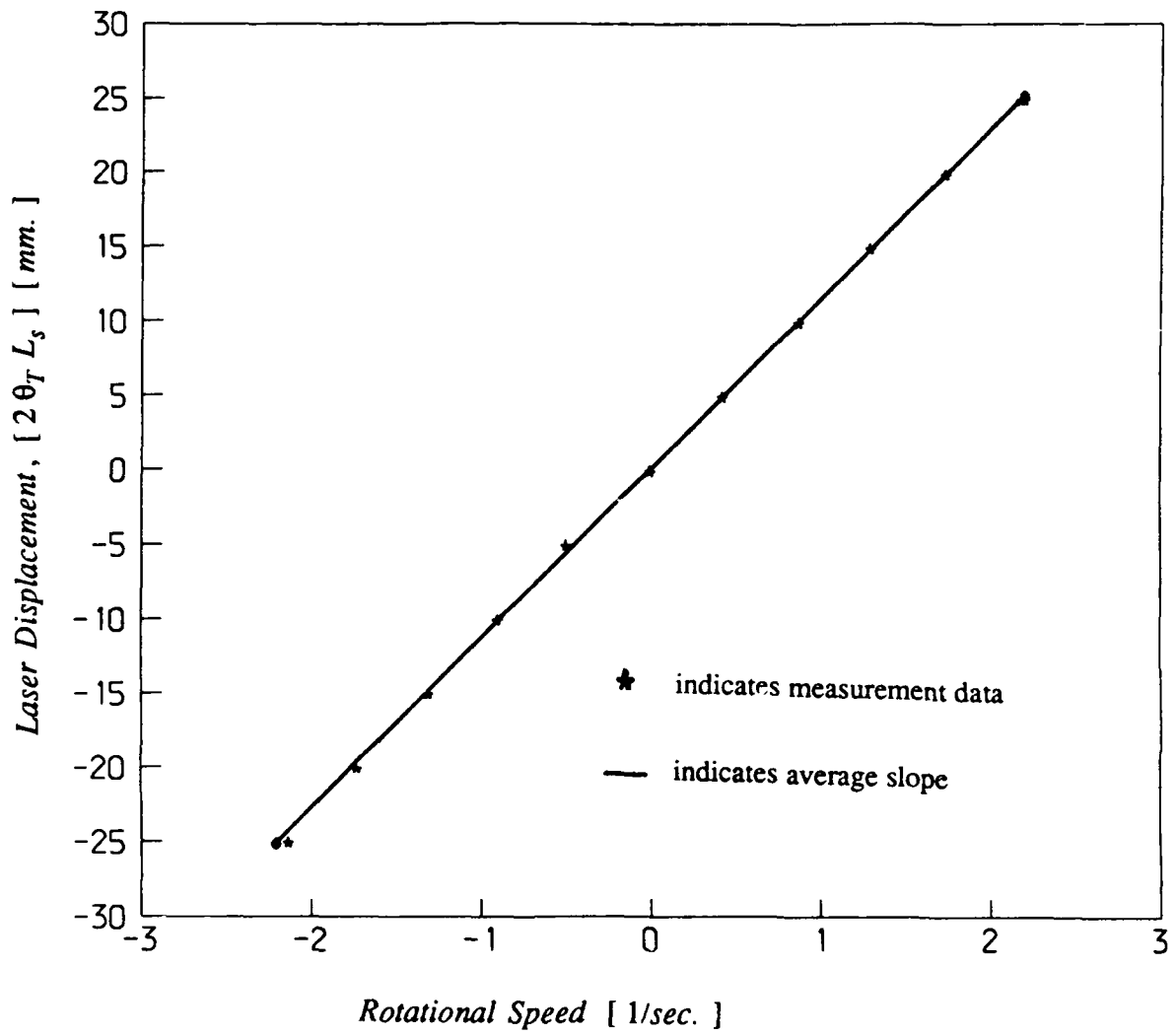
Figure (15). Experimental result for $\frac{H}{d} = 16$, $\beta = 12^0$
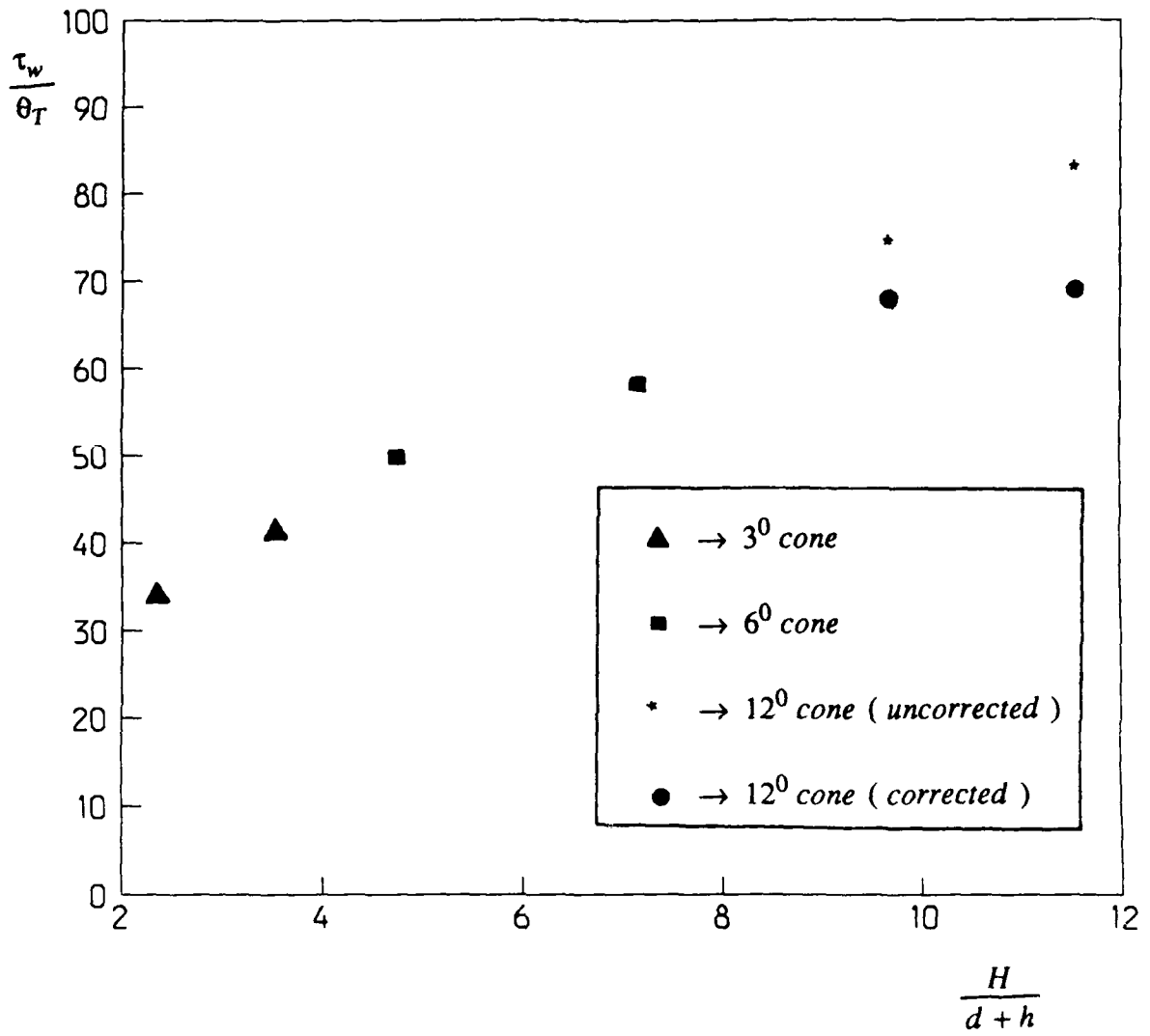
Figure (16). $\dfrac{\tau_w}{\theta_T}$ versus $\dfrac{H}{d+h}$

- 58 -

Rotational Speed,   [1 / sec.]
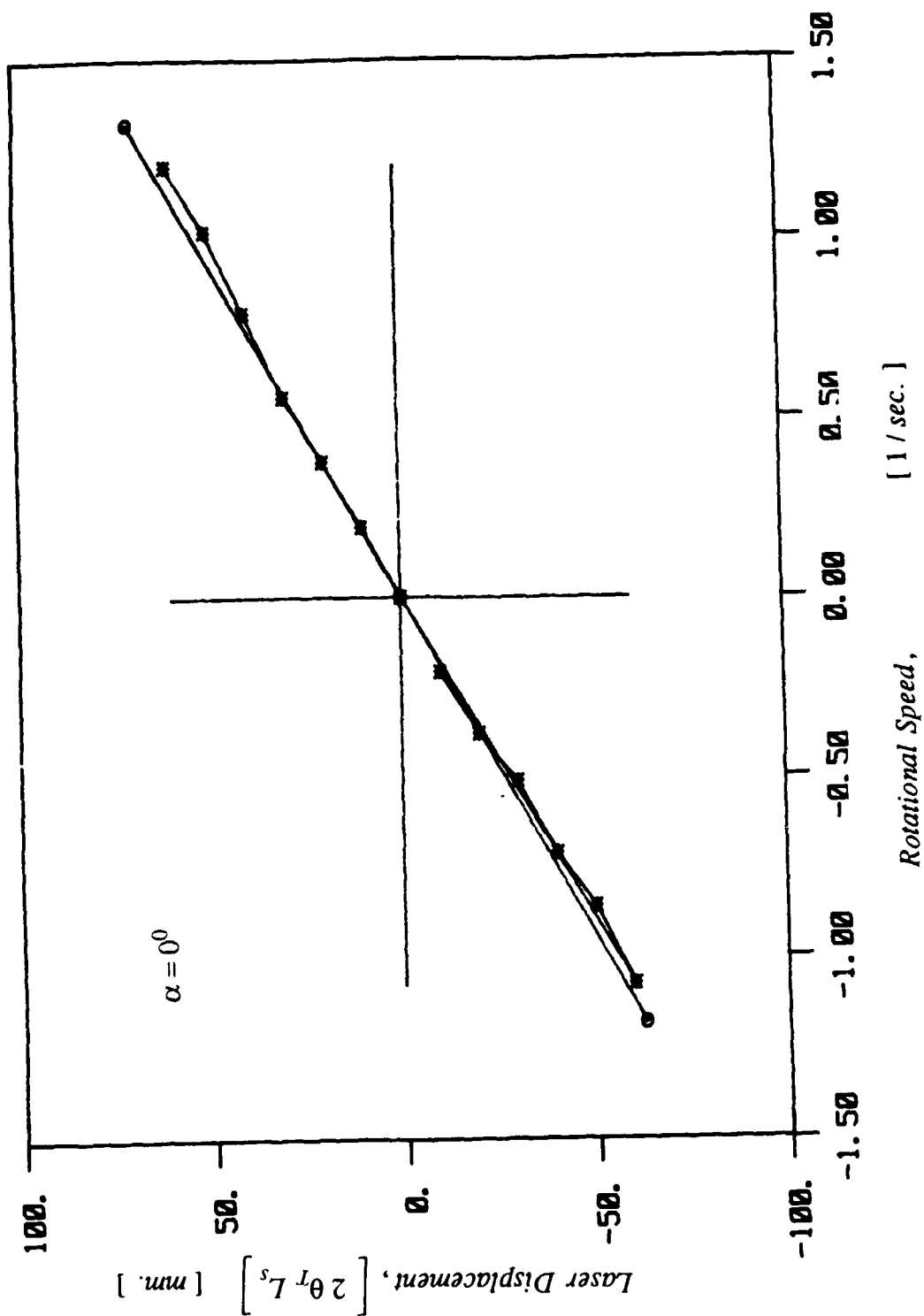
Figure (17). Direction sensitivity for $\alpha = 0^0$

Rotational Speed, [1 / sec.]
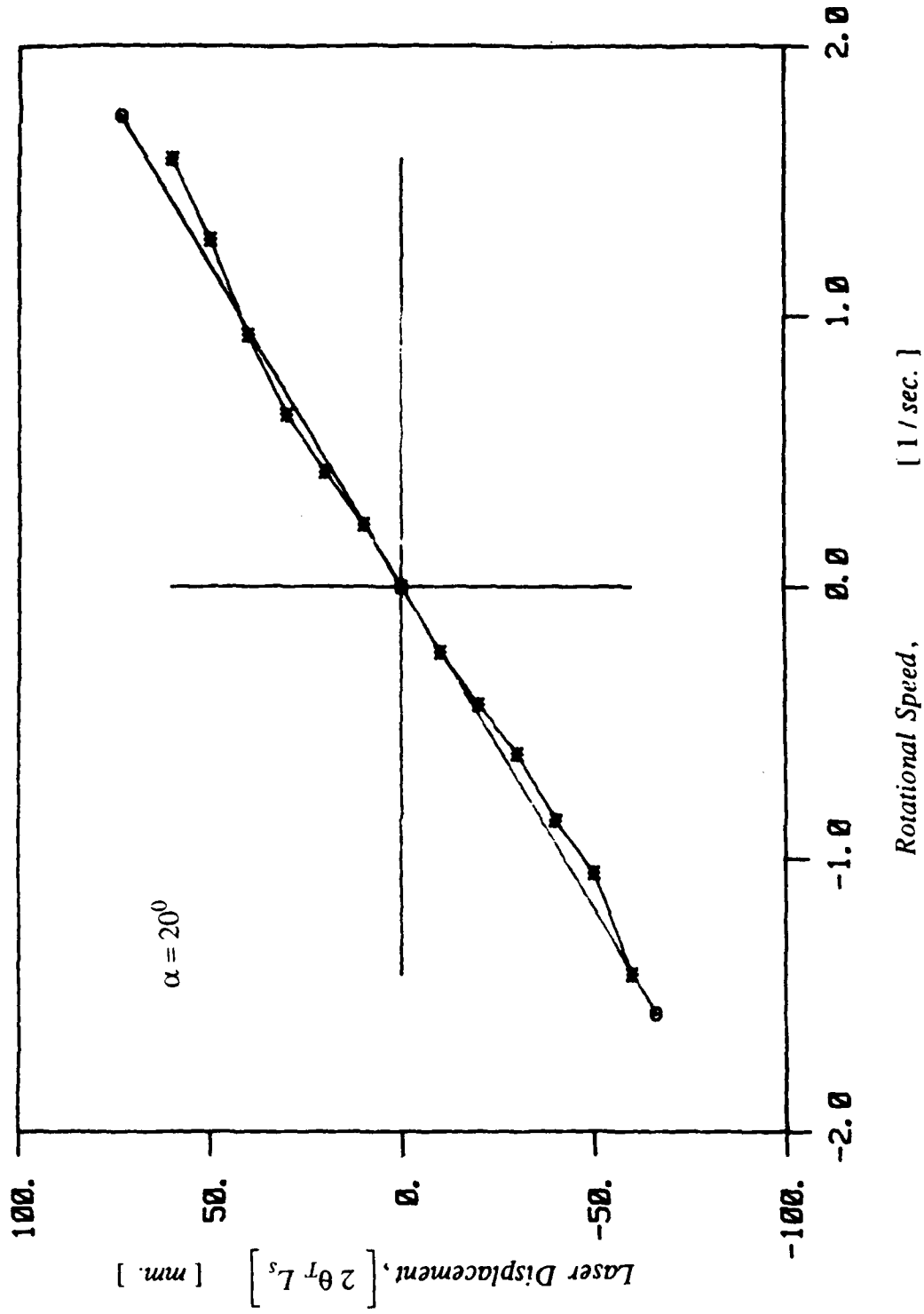
Figure (18). Direction sensitivity for $\alpha = 20^0$

- 60 -

Rotational Speed,   [1 / sec.]
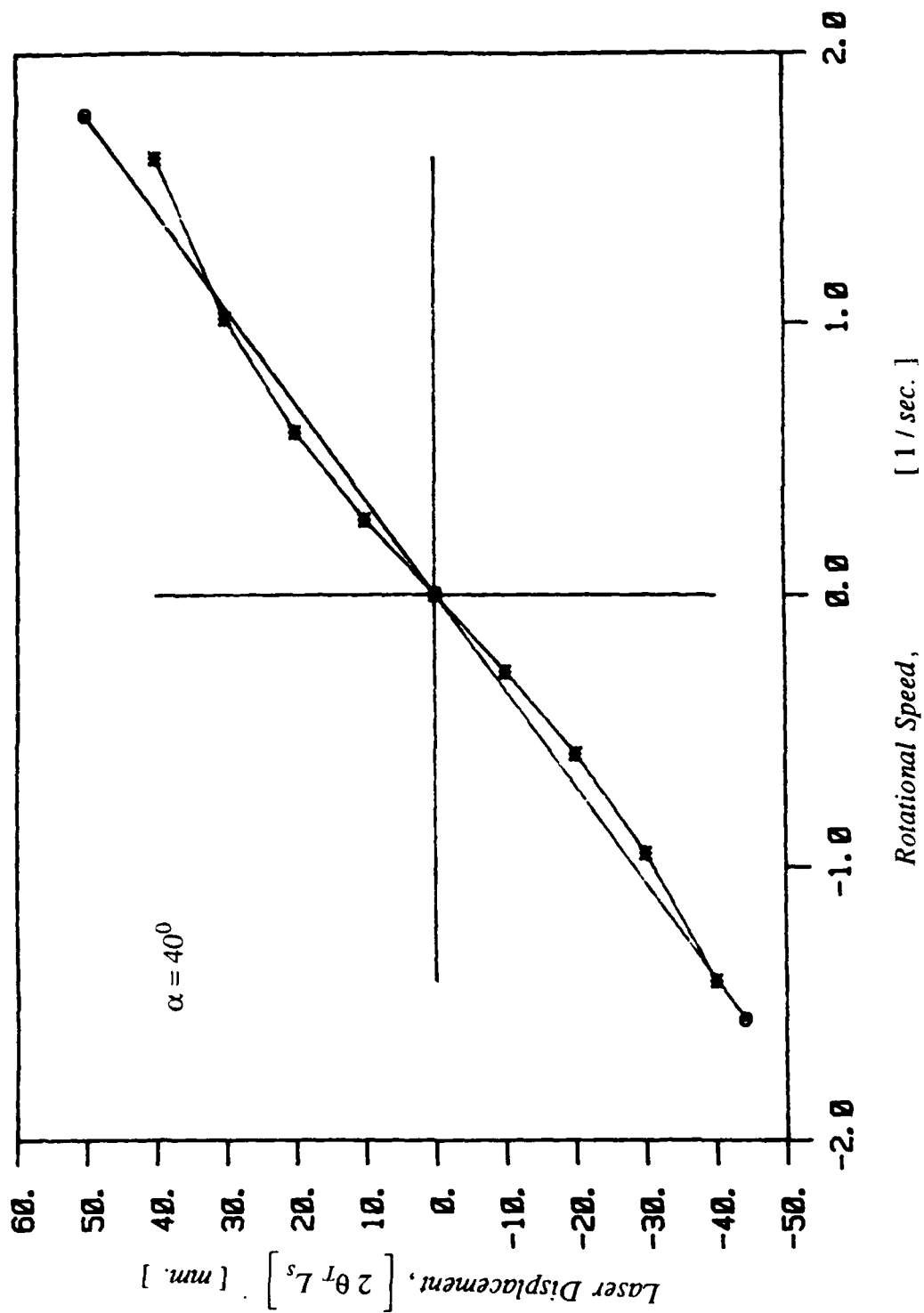
Figure (19). Direction sensitivity for $\alpha = 40^0$

- 61 -
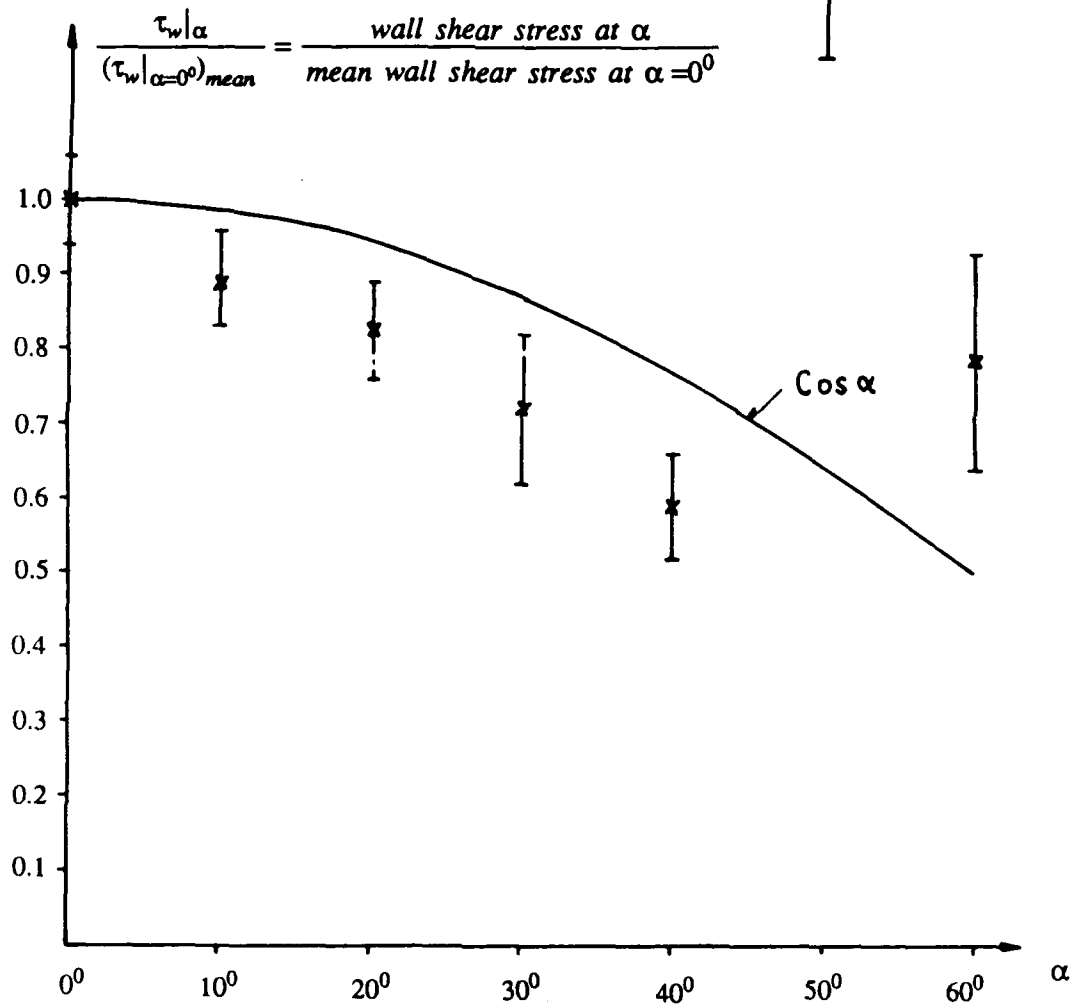
Figure (20). Directivity curve
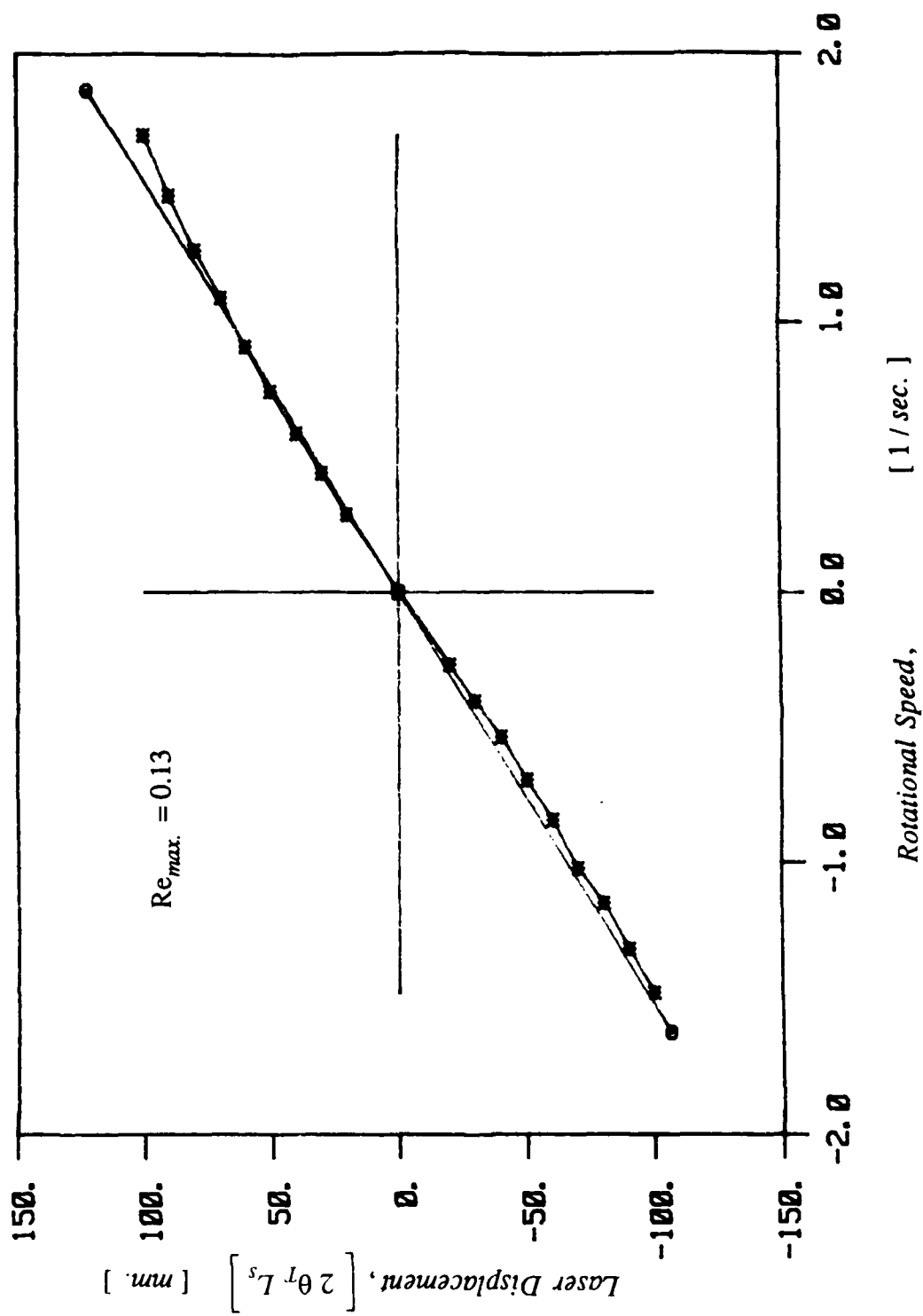
Figure (21). Experimental result for $Re_{max.} = 0.13$
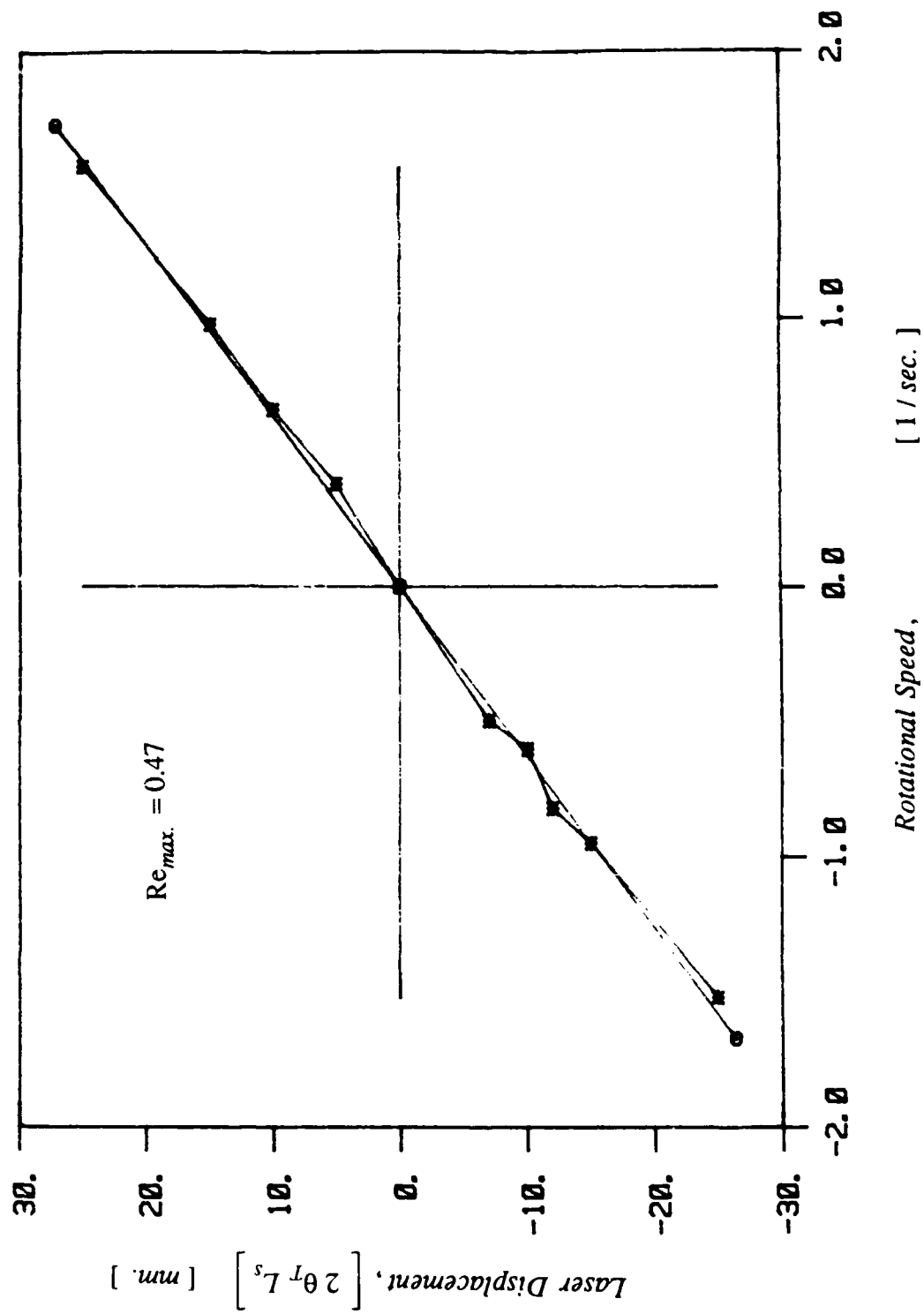
Figure (22). Experimental result for $Re_{max.} = 0.47$
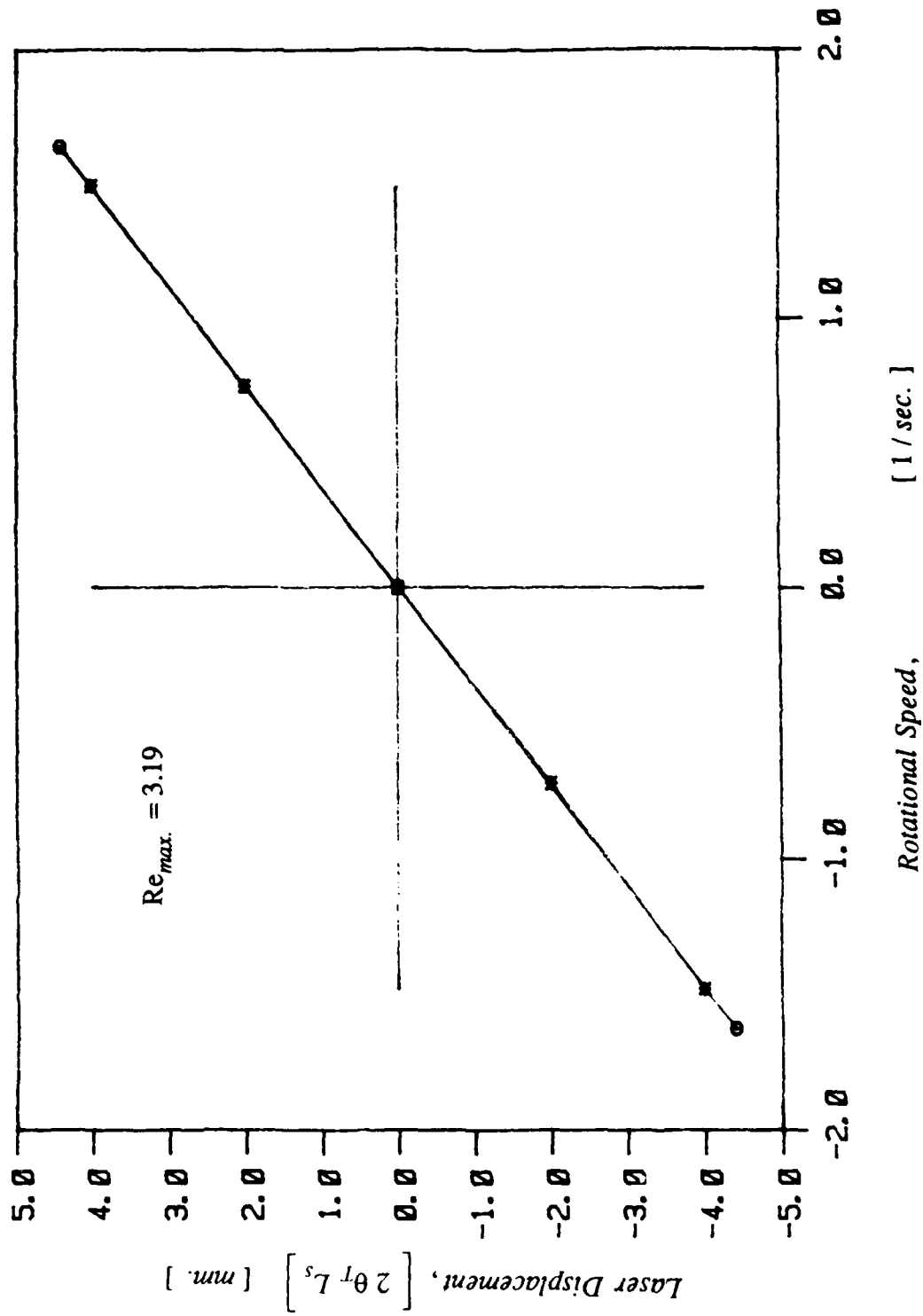
Figure (23). Experimental result for $Re_{max.}$ = 3.19
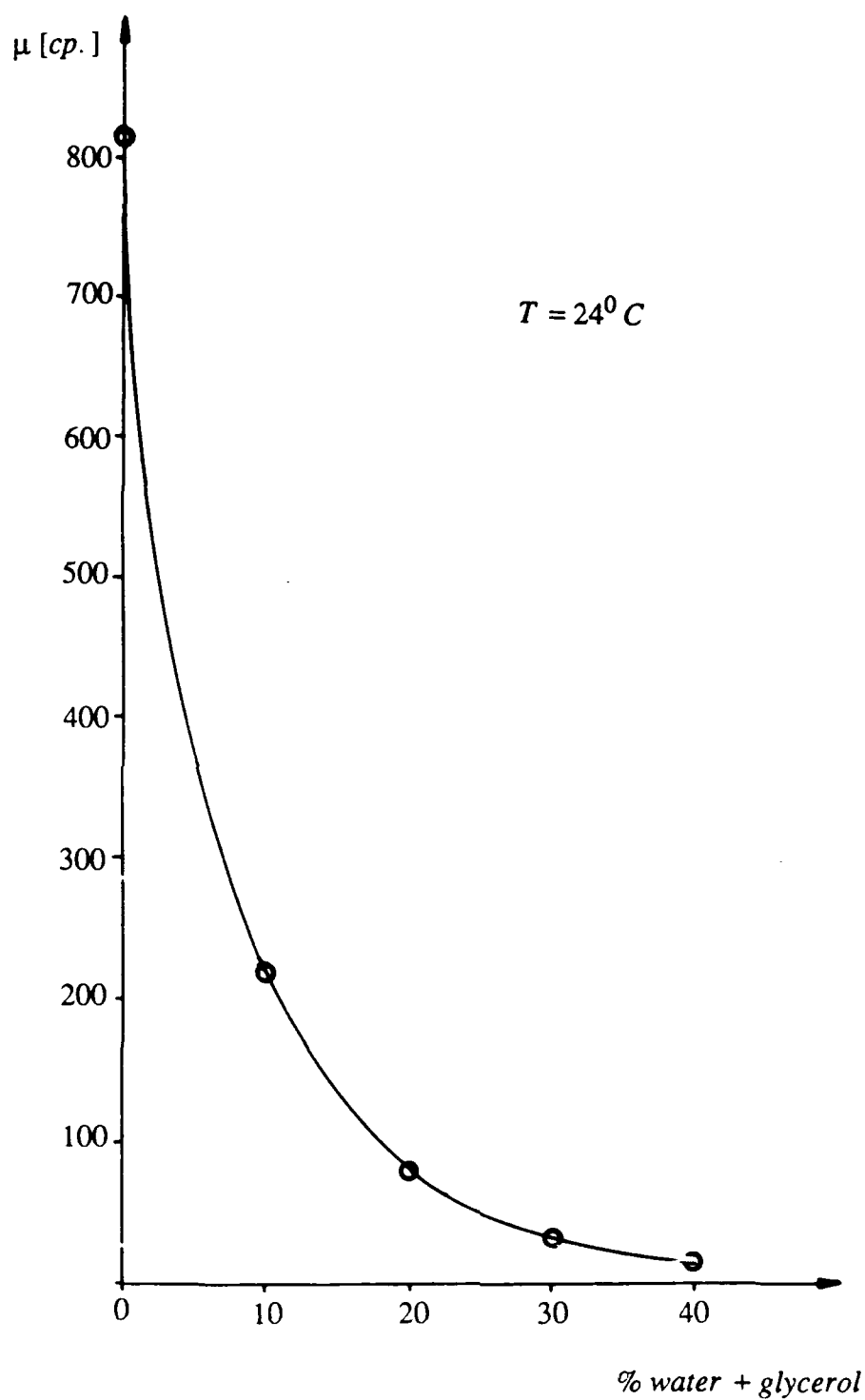
Figure (24). Viscosities of glycerol-water mixtures at $T = 24^0 C$
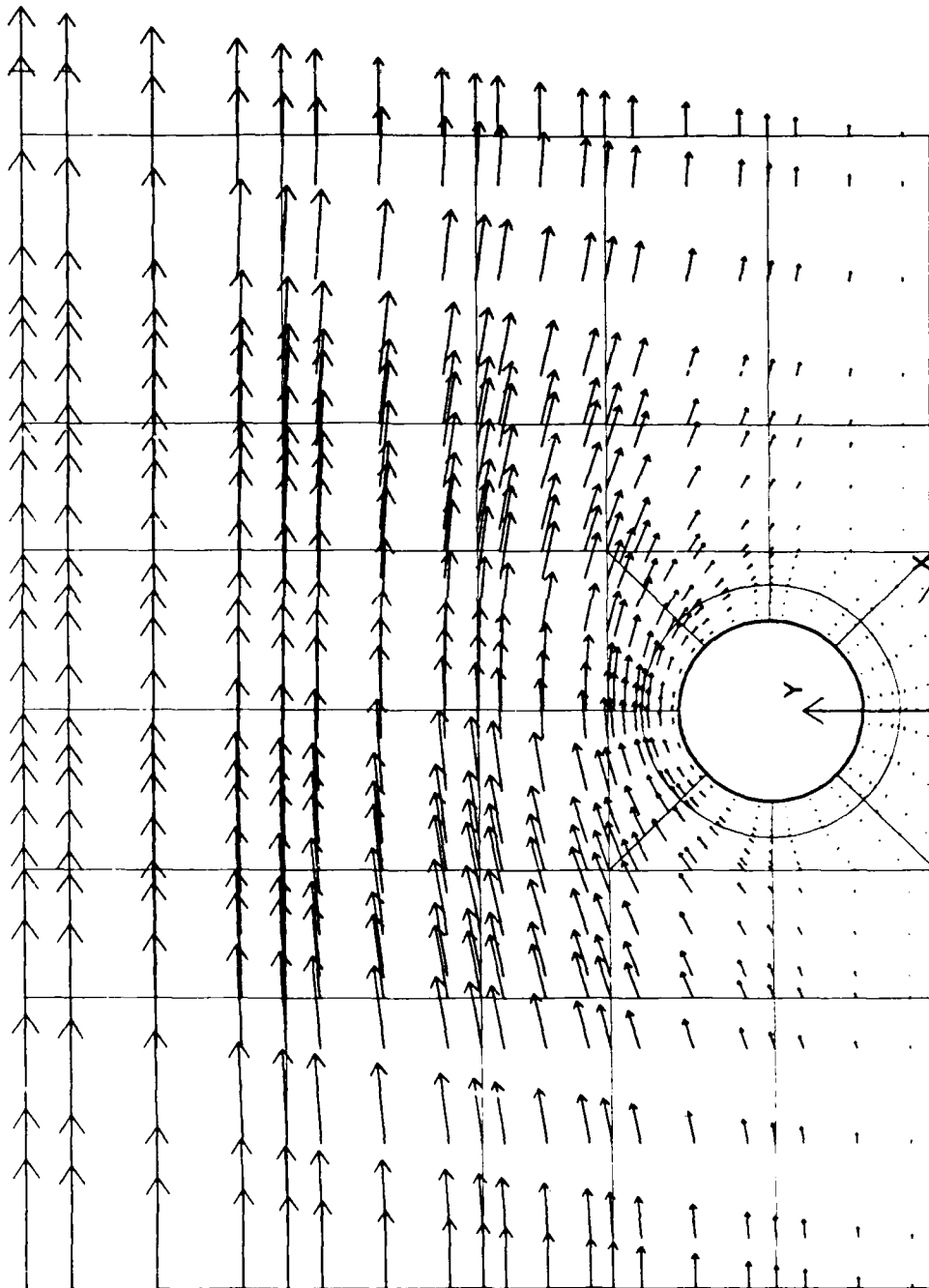
Figure (25). Plot of the velocity field for $\dfrac{H}{d+h} = 3.58$
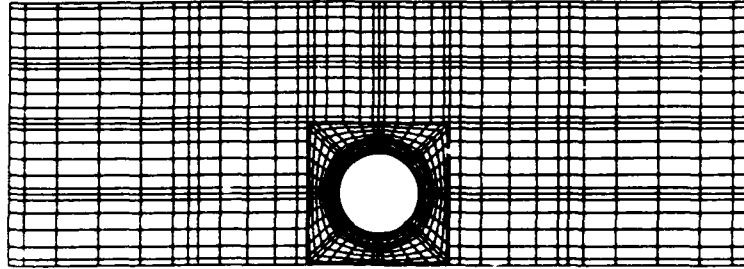
Figure (26). Spectral element mesh for $\dfrac{H}{d+h} = 2.355$
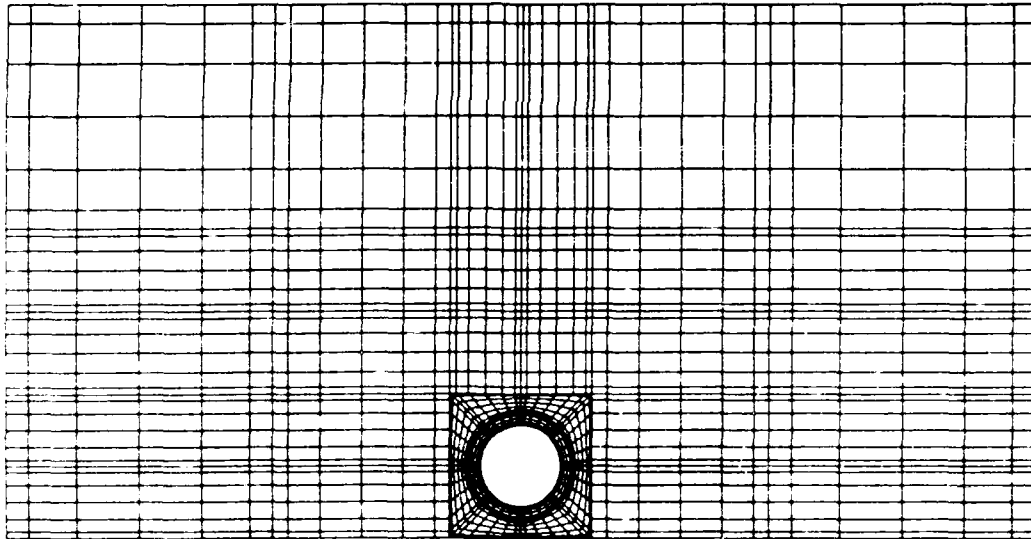
Figure (27). Spectral element mesh for $-\dfrac{H}{d+h} = 4.754$

- 68 -
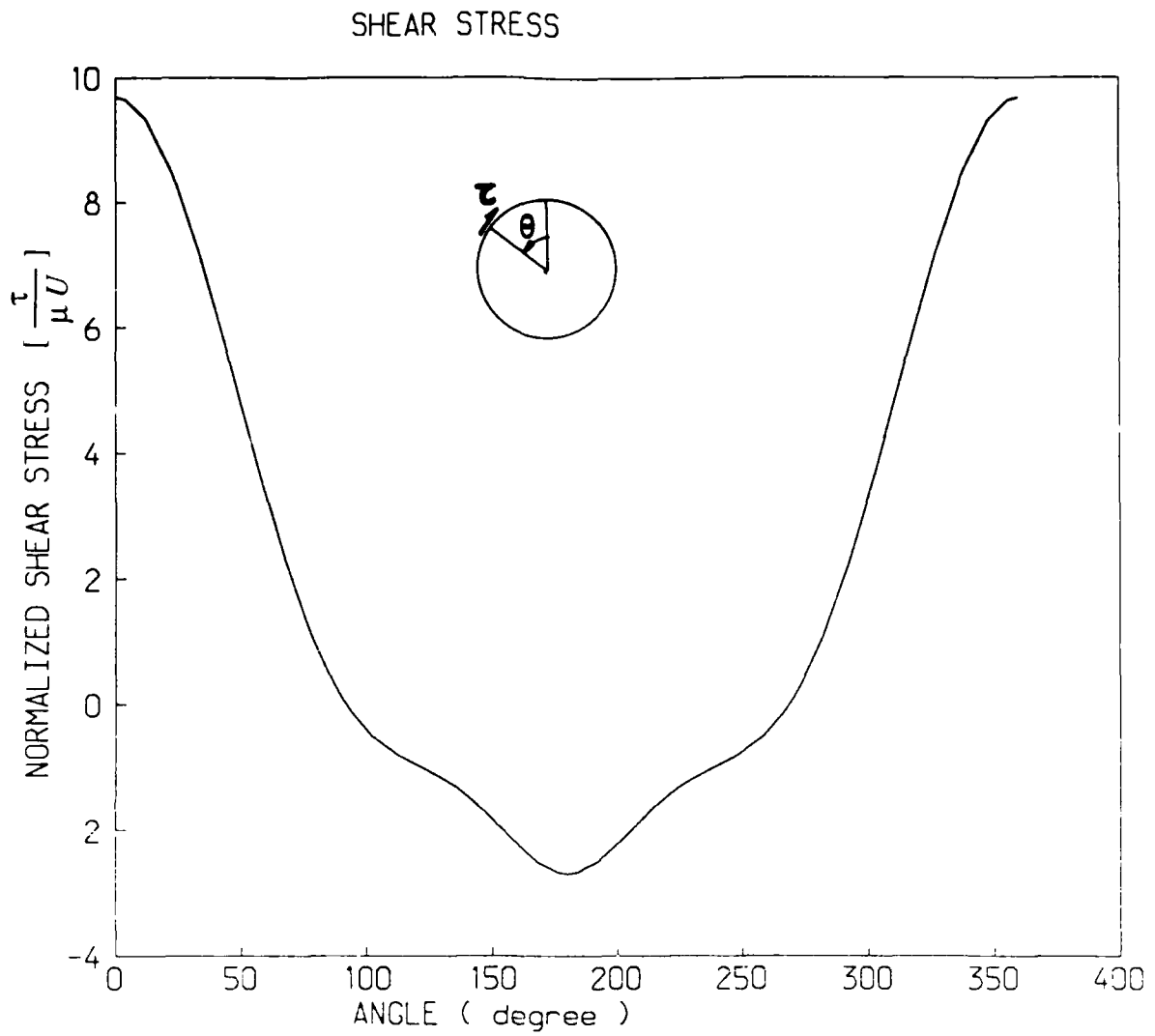
SHEAR STRESS

Figure (28). Shear stress distribution on the cylinder for $\dfrac{H}{d \div h} = 2.355$
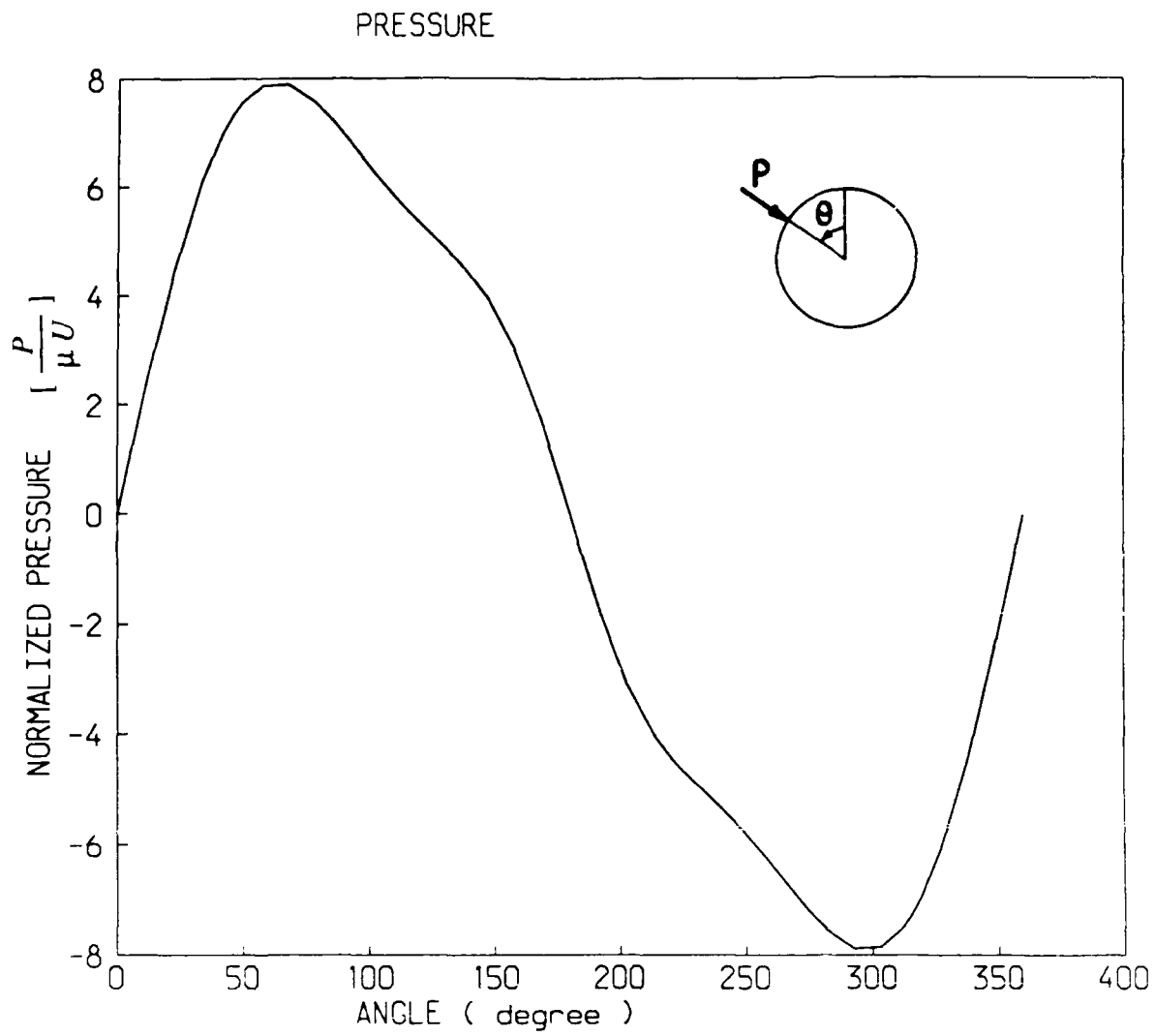
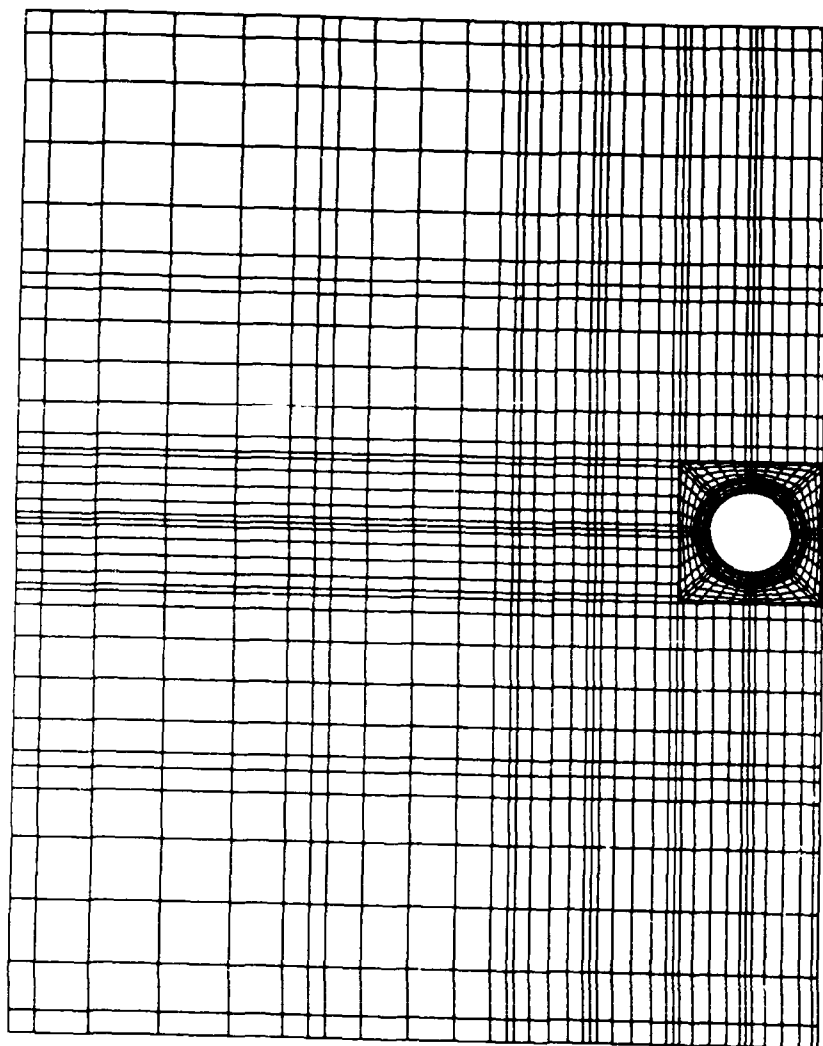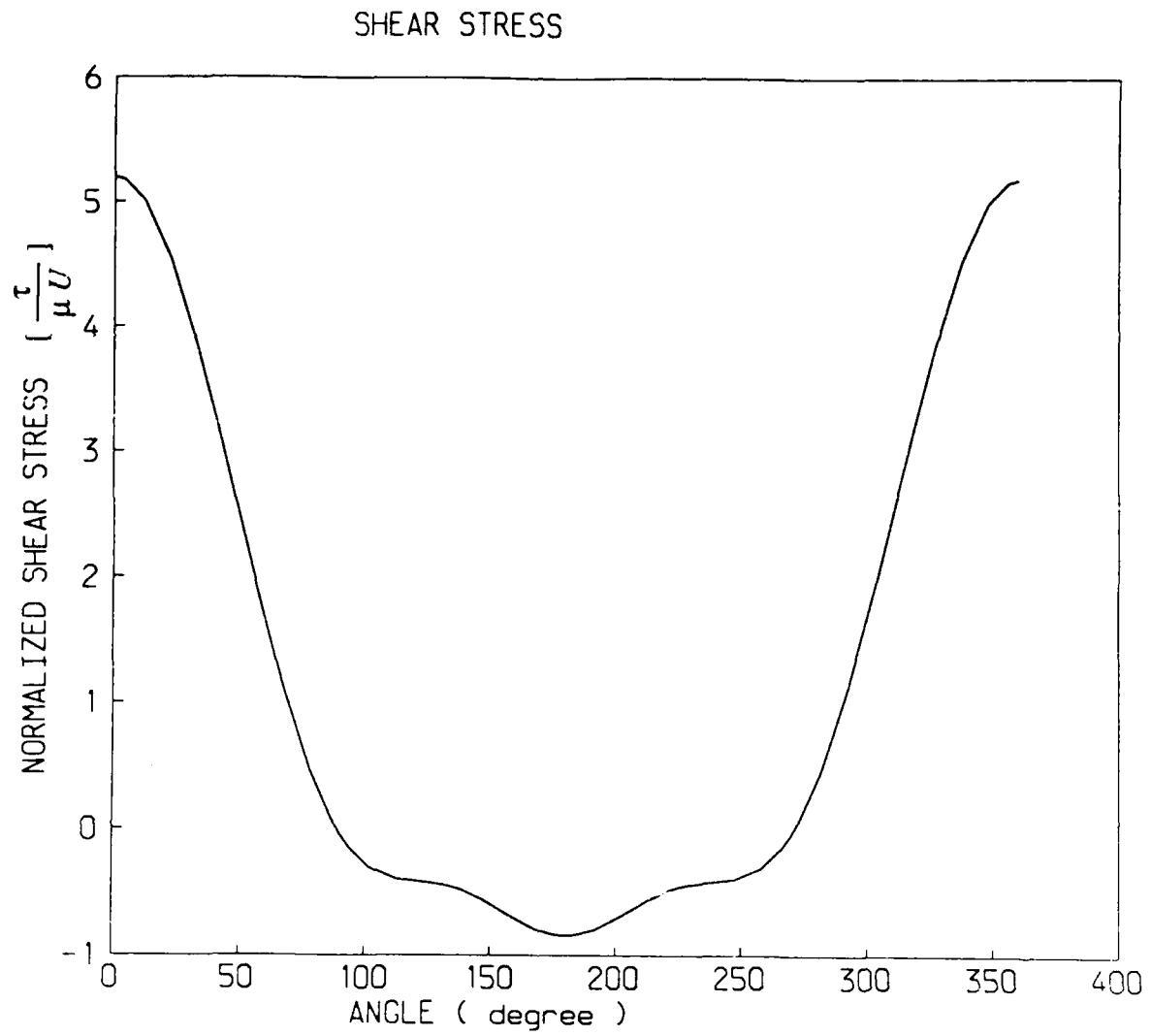Figure (29). Pressure distribution on the cylinder for $\dfrac{H}{d+h} = 2.355$
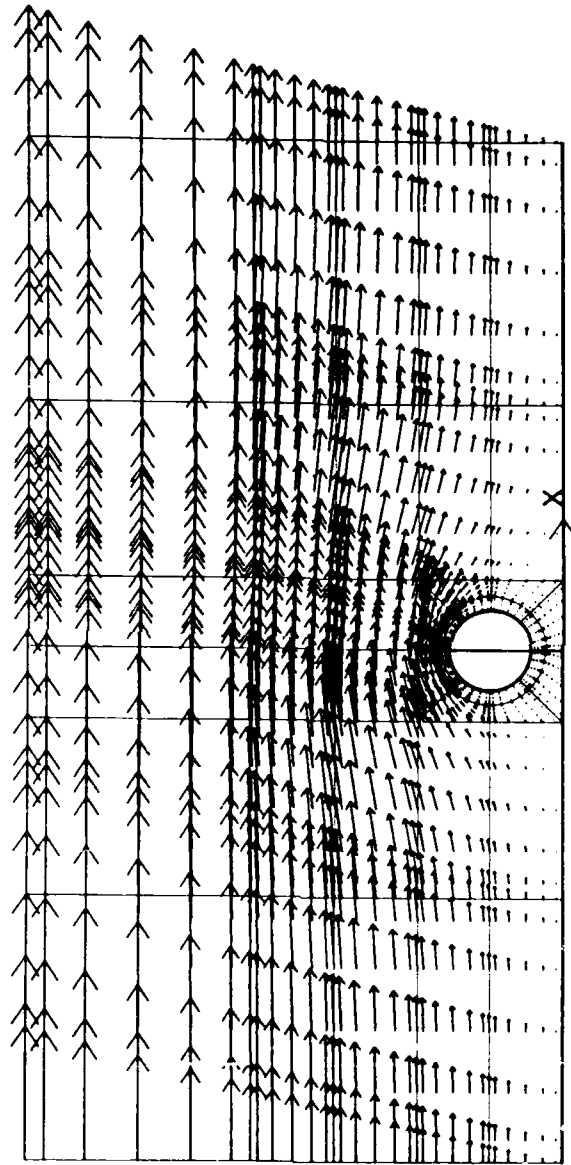
Figure (30). Plot of the velocity field for $\dfrac{H}{d+h} = 4.754$
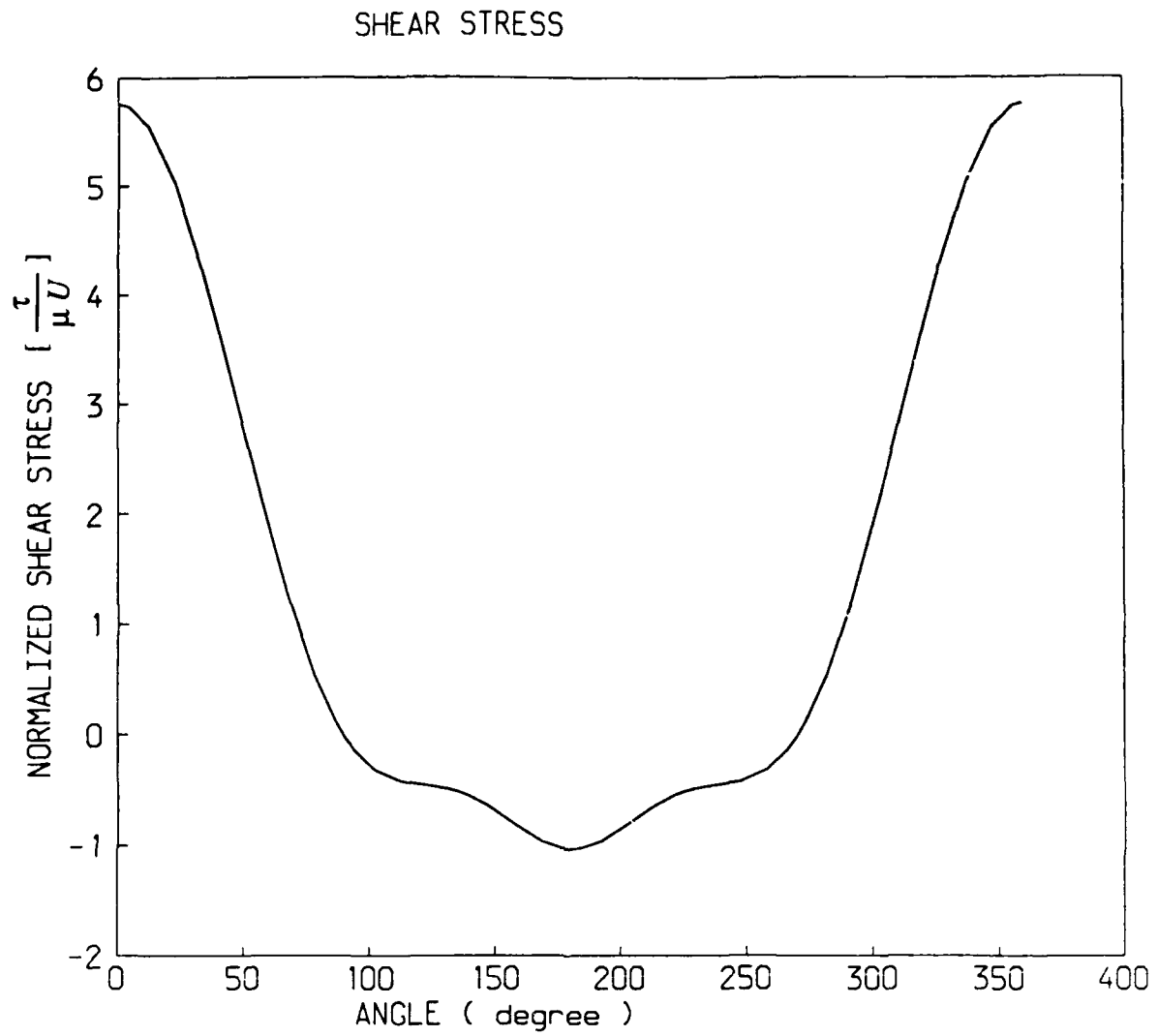
SHEAR STRESS

Figure (31). Shear stress distribution on the cylinder for $\dfrac{H}{d+h} = 4.754$
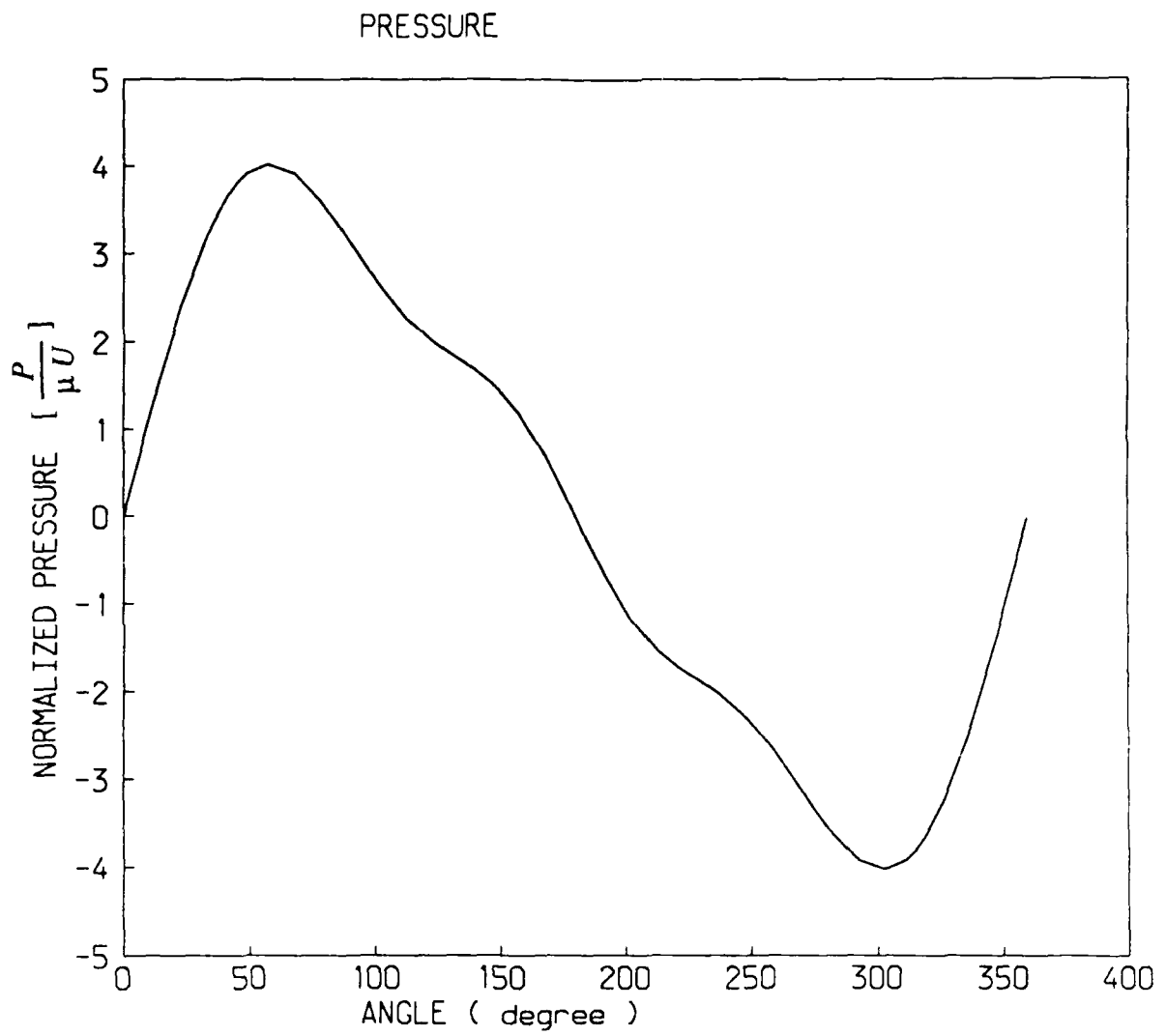
PRESSURE
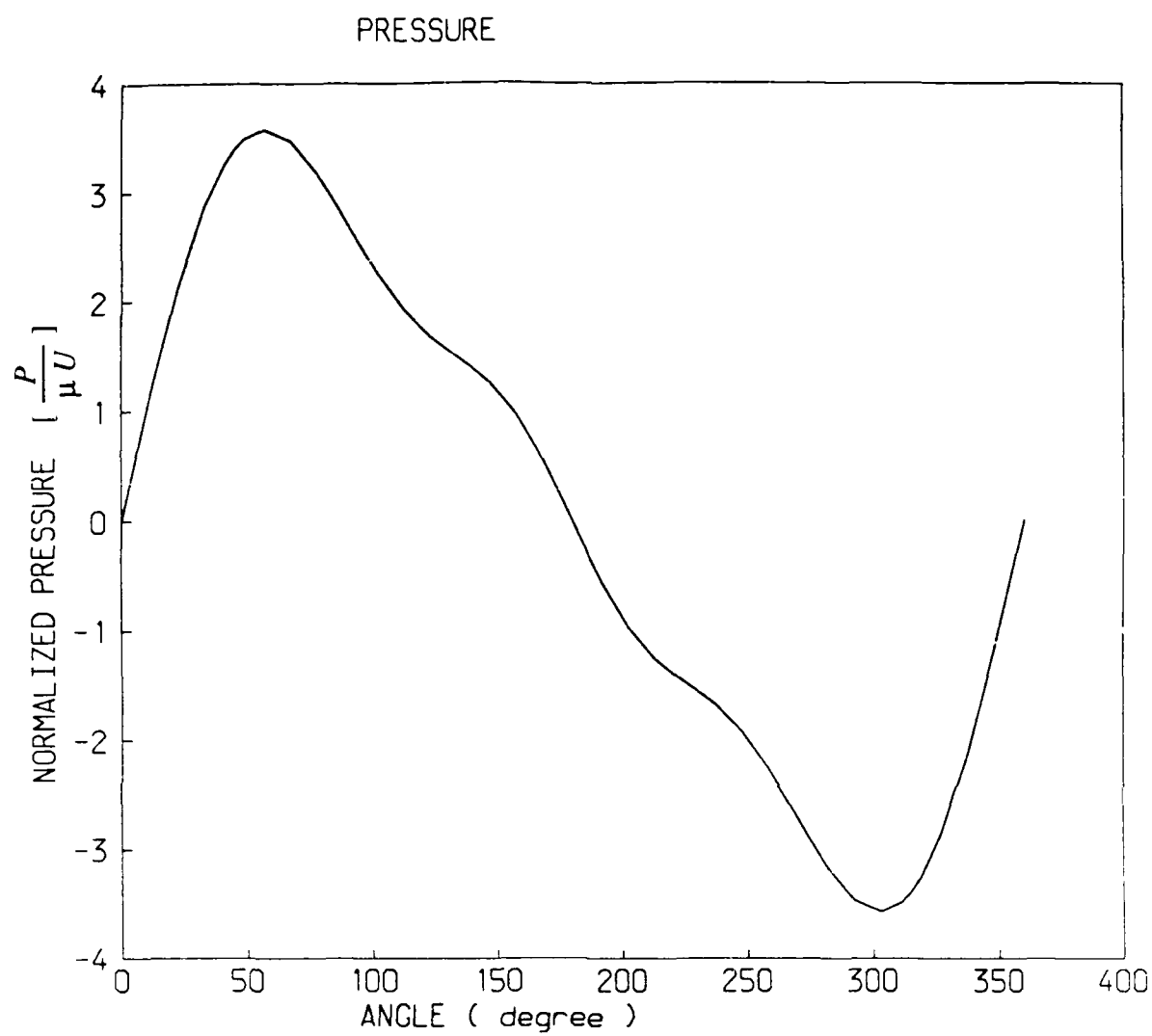

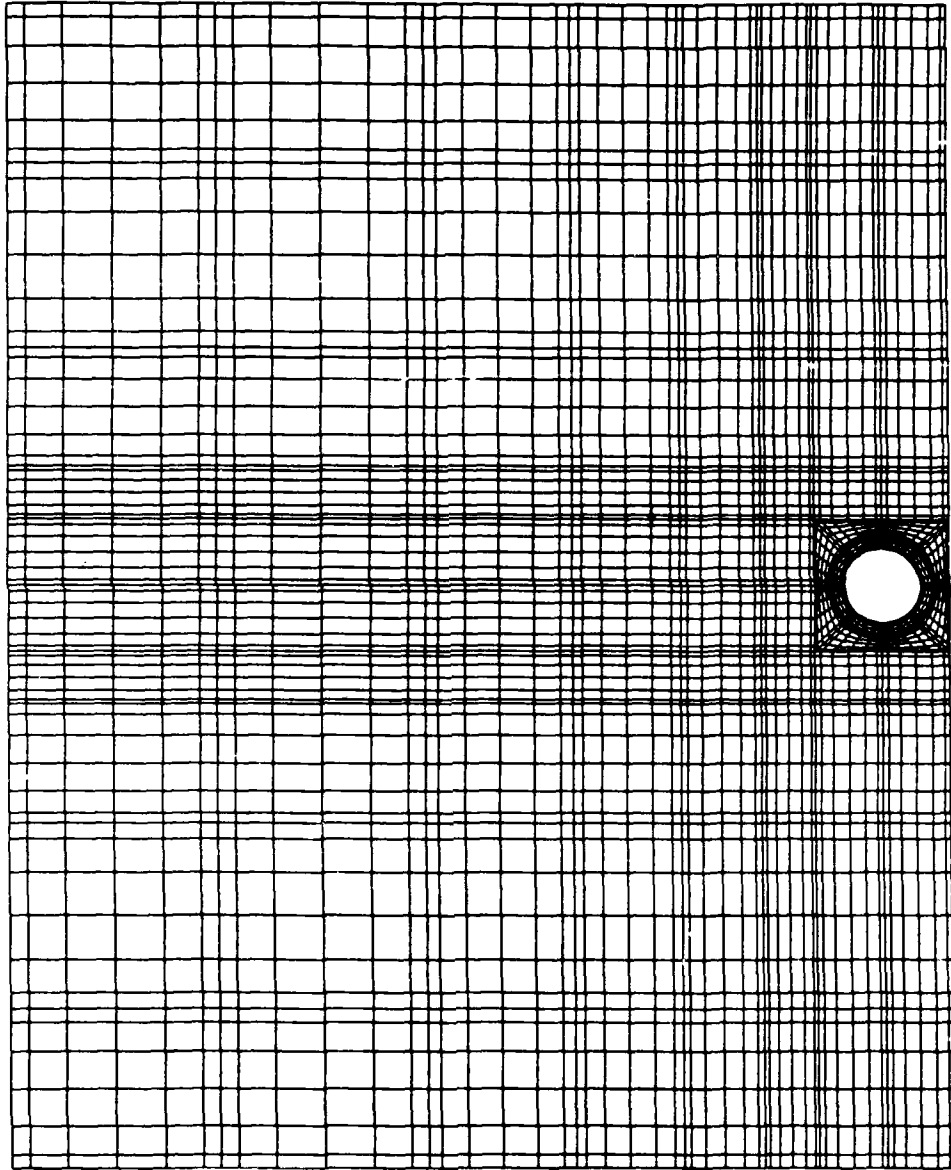Figure (32). Pressure distribution on the cylinder for $\dfrac{H}{d+h} = 4.754$

Figure (33). Spectral element mesh for $\dfrac{H}{d+h} = 7.167$

SHEAR STRESS

Figure (34). Shear stress distribution on the cylinder for $\dfrac{H}{d+h} = 7.167$

PRESSURE

Figure (35). Pressure distribution on the cylinder for $\dfrac{H}{\mathit{d}+h} = 7.167$

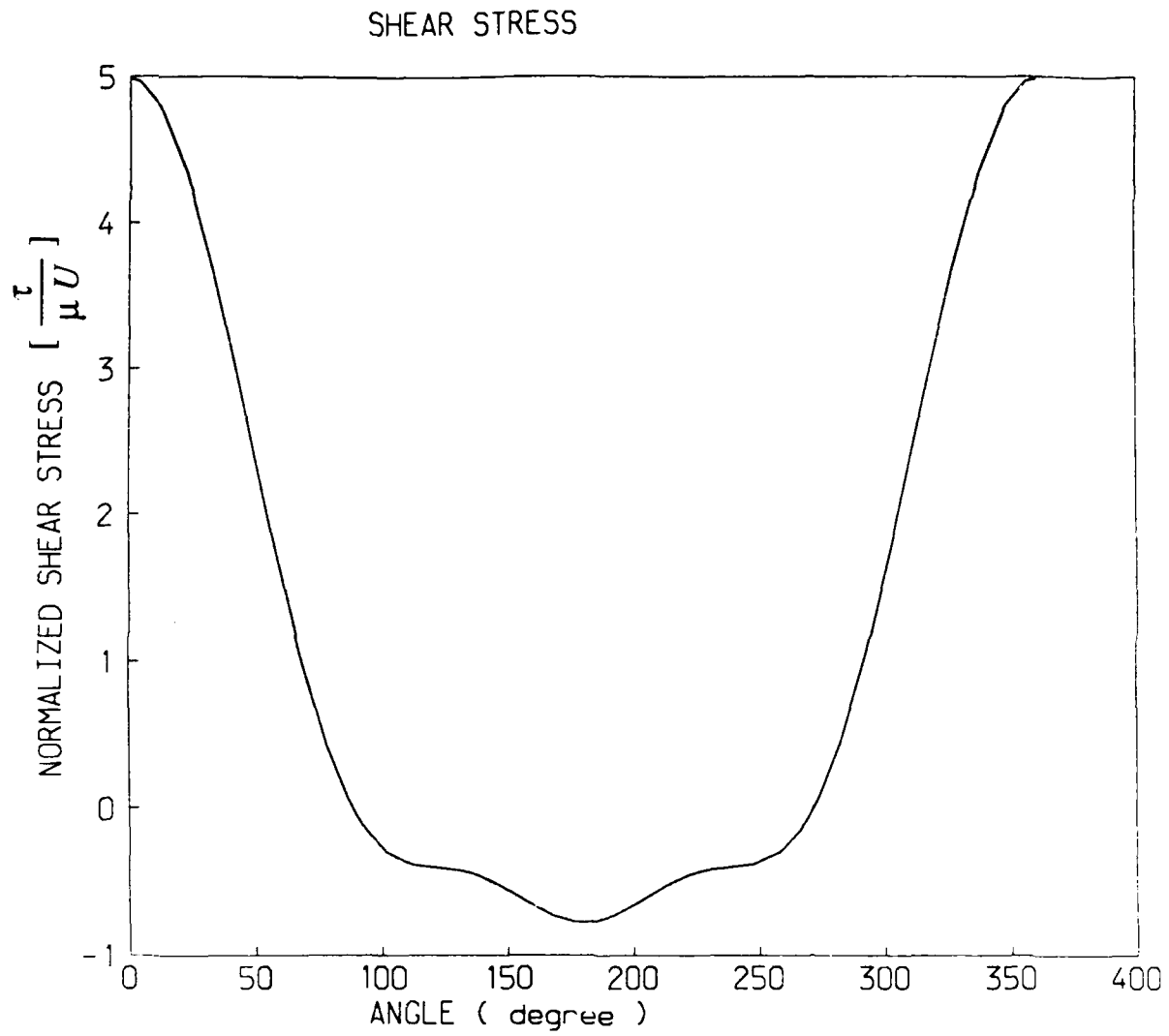Figure (36). Spectral element mesh for $\dfrac{H}{d+h} = 8.94$

SHEAR STRESS

Figure (37). Shear stress distribution on the cylinder for $\dfrac{H}{d+h} = 8.94$
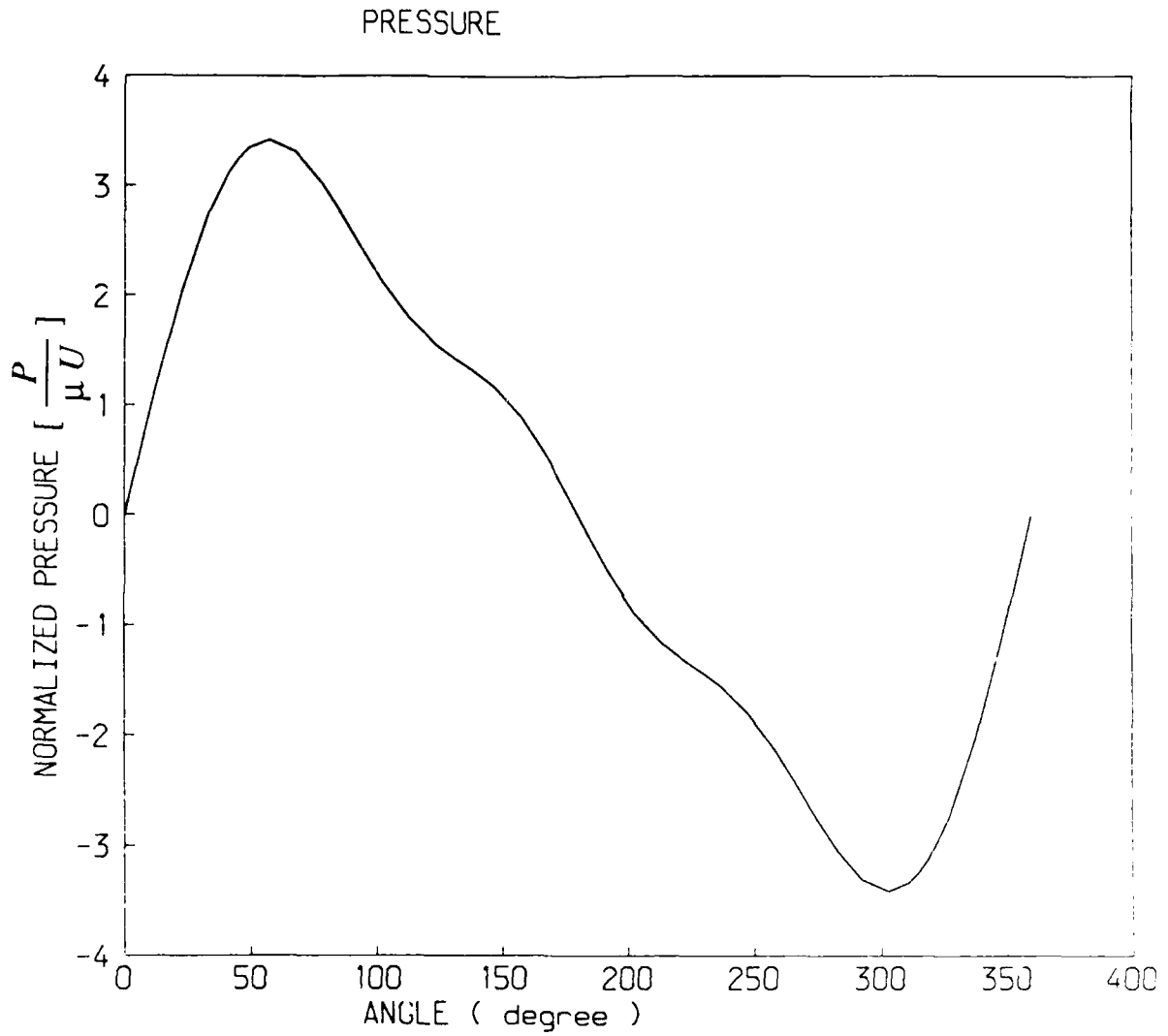
PRESSURE

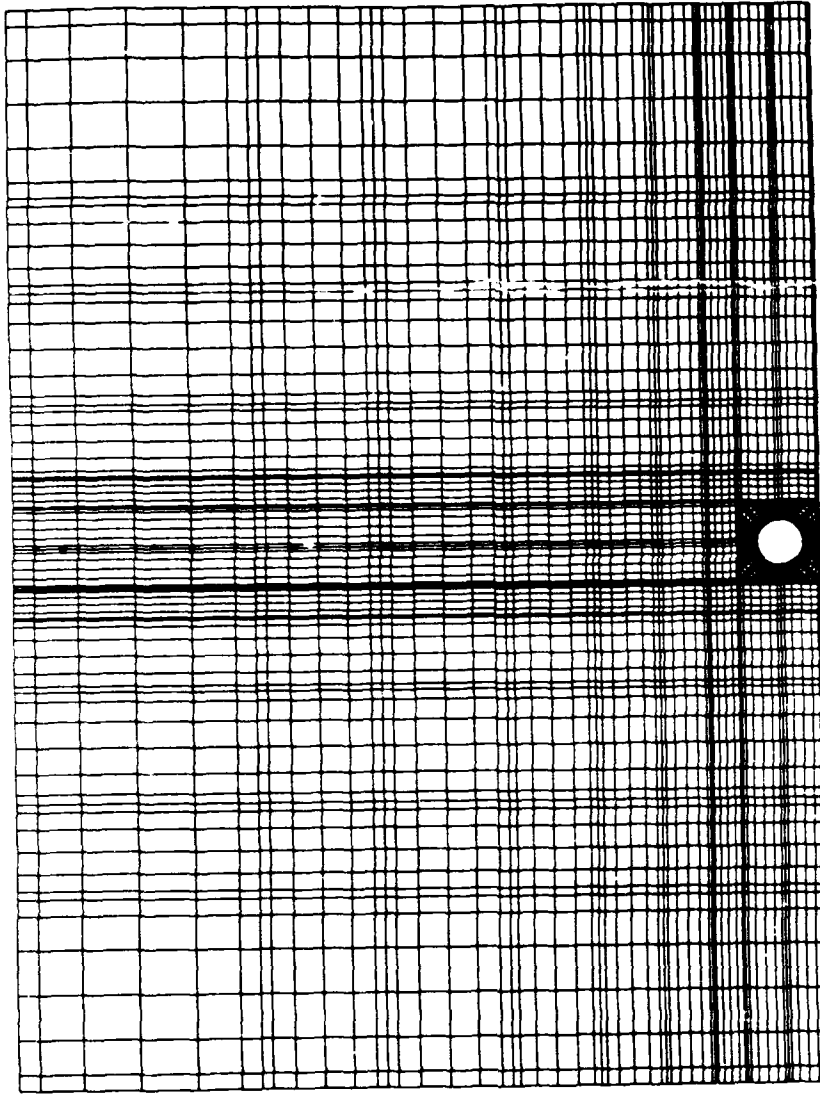Figure (38). Pressure distribution on the cylinder for $\dfrac{H}{d+h} = 8.94$

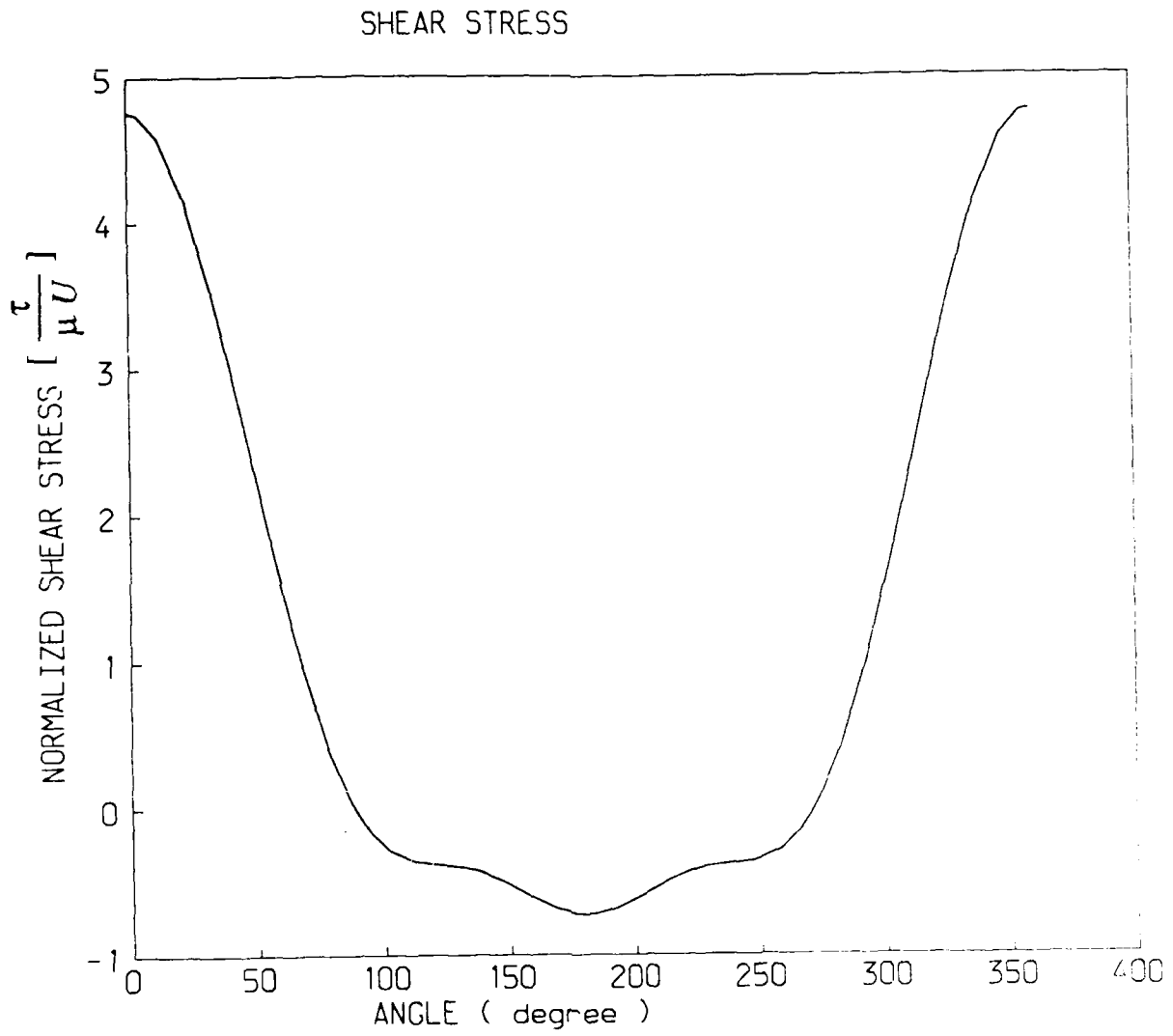Figure (39). Spectral element mesh for $\dfrac{H}{a+h} = 12.77$

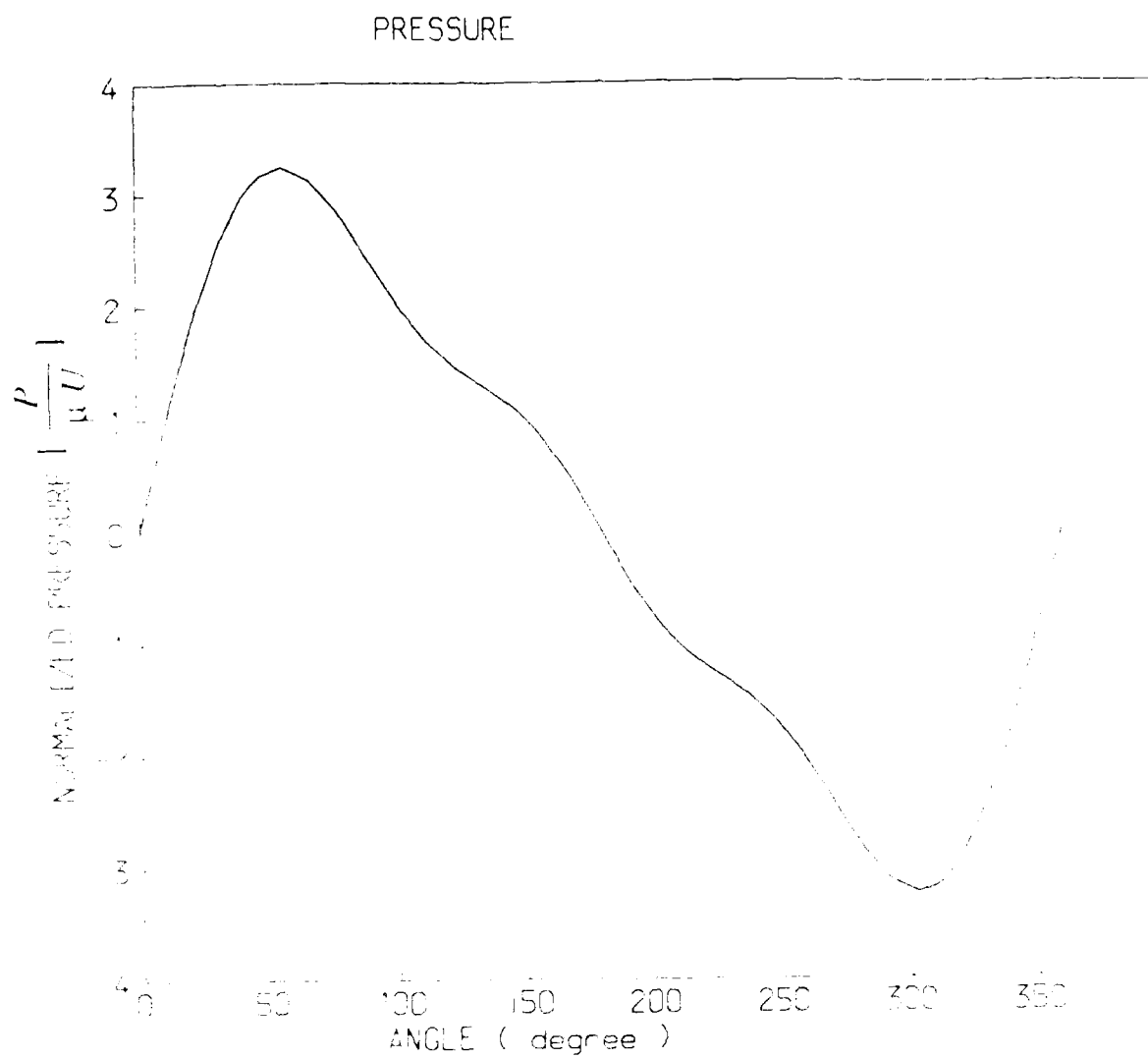Figure (40). Shear stress distribution on the cylinder for $\dfrac{H}{d+h} = 12.77$

PRESSURE

Figure (41). Pressure distribution on the cylinder for $\dfrac{H}{d + n} = 12\ 77$

$\dfrac{H}{d+h}$	2.355	3.58	4.754	4.98	7.167	8.94	12.77
η_t	1.941	1.505	1.259	1.238	1.143	1.095	1.044
η_d	2.651	1.673	1.318	1.293	1.162	1.106	1.048
$\dfrac{\tau_{max.}}{\tau_w}$	9.684	6.686	5.758	5.602	5.197	4.985	4.761
$\dfrac{\tau_{min.}}{\tau_w}$	-2.698	-1.291	-1.041	-0.730	-0.847	-0.778	-0.726
$\dfrac{p_{max.}}{\tau_w}$	7.886	5.029	4.022	3.880	3.577	3.418	3.246

TABLE (1). Computational Results

$\dfrac{H}{d}$	3.26	4.91	6.58	9.92	13.4	16
$\dfrac{H}{d+h}$	2.355	3.548	4.754	7.167	9.68	11.54
$\beta\,[deg.]$	3	3	6	6	12	12
$\dfrac{\tau_w}{\theta_{T\ exp.}}$	34.30	41.49	50.01	58.48	74.95	83.50
$\dfrac{\tau_w}{\theta_{T\ corrected}}$	-	-	-	-	68.20	69.30

TABLE (2). Experimental Results